

1 **Modeling the timing of Patagonian Ice Sheet retreat in the Chilean Lake District from 22-**
2 **10 ka**

3
4 Joshua Cuzzone¹, Matias Romero², Shaun A. Marcott²

5
6 ¹Joint Institute for Regional Earth System Science and Engineering, University of California, Los
7 Angeles

8 ²Department of Geoscience, University of Wisconsin, Madison

9
10 *Correspondence to:* Joshua K. Cuzzone (Joshua.K.Cuzzone@jpl.nasa.gov)

11 **Abstract**

12
13 Studying the retreat of the Patagonian Ice Sheet (PIS) during the last deglaciation represents an
14 important opportunity to understand how ice sheets outside the polar regions have responded to
15 deglacial changes in temperature and large-scale atmospheric circulation. At the northernmost
16 extension of the PIS during the last glacial maximum (LGM), the Chilean Lake District (CLD)
17 was influenced by the southern westerly winds (SWW), which strongly modulated the hydrologic
18 and heat budget of the region. Despite progress in constraining the nature and timing of deglacial
19 ice retreat across this area, considerable uncertainty in the glacial history still exists due to a lack
20 of geologic constraints on past ice margin change. Where the glacial chronology is lacking, ice
21 sheet models can provide important insight into our understanding of the characteristics and drivers
22 of deglacial ice retreat. Here we apply the Ice Sheet and Sea-level System Model (ISSM) to
23 simulate the LGM and last deglacial ice history of the PIS across the CLD at high spatial resolution
24 (450 meters). We present a transient simulation of ice margin change across the last deglaciation
25 using climate inputs from the CCSM3 Trace-21ka experiment. At the LGM, the simulated ice
26 extent across the CLD agrees well with the most comprehensive reconstruction of PIS ice history
27 (PATICE). Coincident with deglacial warming, ice retreat ensues after 19ka, with largescale ice
28 retreat occurring across the CLD between 18 and 16.5 ka. By 17 ka the northern portion of the
29 CLD becomes ice free, and by 15 ka, ice only persists at high elevations as mountain glaciers and
30 small ice caps. Our simulated ice history agrees well with PATICE for early deglacial ice retreat
31 but diverges at and after 15 ka, where the geologic reconstruction suggests persistence of an ice
32 cap across the southern CLD until 10 ka. However, given the high uncertainty in the geologic
33 reconstruction of the PIS across the CLD during the later deglaciation, this work emphasizes a
34 need for improved geologic constraints on past ice margin change. While deglacial warming drove
35 the ice retreat across this region, sensitivity tests reveal that modest variations in wintertime
36 precipitation (~10%) can modulate the pacing of ice retreat by up to 2 ka, which has implications
37 when comparing simulated outputs of ice margin change to geologic reconstructions. While we
38 find that TraCE-21ka simulates large-scale changes in the SWW across the CLD that are consistent
39 with regional paleoclimate reconstructions, the magnitude of the simulated precipitation changes
40 is smaller than what is found in proxy records. From our sensitivity analysis we can deduce that
41 larger anomalies in precipitation as found in paleoclimate proxies may have had a large impact on
42 modulating deglacial ice retreat, highlighting an additional need to better constrain the deglacial
43 change in the strength, position, and extent of the SWW as it relates to understanding the drivers
44 of deglacial PIS behavior.

46 **1 Introduction**

47
48 During the Last glacial maximum (LGM), the Patagonian Ice Sheet (PIS) covered the Andes
49 mountains from 38°S to 55°S, with an estimated sea-level equivalent ice volume of 1.5 meters
50 (Davies et al., 2020). At the northernmost extent of the PIS, across an area presently known as the
51 Chilean Lake District (CLD; 37°S-41.5°S), the LGM to deglacial ice behavior and related climate
52 forcings has been a subject of historical interest (Mercer, 1972; Porter, 1981; Lowell et al., 1995;
53 Andersen et al., 1999; Denton et al., 1999; Glasser et al., 2008, Moreno et al., 2015; Kilian and
54 Lamy, 2012; Lamy et al., 2010), and have served as important constraints towards understanding
55 the drivers of ice sheet change across centennial to millennial timescales. Currently, PATICE
56 (Davies et al., 2020) serves as the latest and most complete reconstruction of the entire PIS during
57 the LGM and last deglaciation. Across the CLD (Figure 1), the LGM ice limits are only well
58 constrained by terminal moraines in the southwest and western margins (Denton et al., 1999;
59 Glasser et al., 2008, Moreno et al., 2015). However, due to a lack of geomorphological and
60 geochronologic constraints on ice margin change following the LGM, the reconstructed
61 deglaciation remains highly uncertain.

Deleted: past

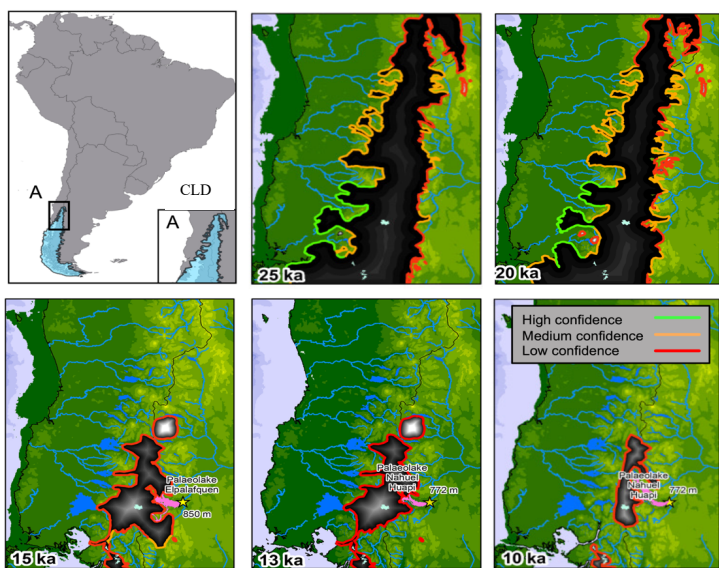


Figure 1. Location of the study area across the Chilean Lake District (CLD; Upper Left Panel). The reconstructed ice extent from PATICE for the PIS across the CLD at 25 ka, 20 ka, 15 ka, 13 ka, and 10 ka are taken from Davies et al., 2020. The color of the line marking the reconstructed ice extent corresponds to the confidence in the reconstruction as described in section 3.3.

62 While deglacial warming is a primary driver of ice retreat across the CLD, evidence suggests that
63 variations in precipitation patterns influenced the timing and magnitude of this retreat (Moreno et
64 al., 1999; Rojas et al., 2009). The wintertime climate across South America is strongly influenced
65 by the southern annular mode (SAM; Hartmann and Lo, 1998), for which its phase and strength is
66 regulated by changes in the difference of zonal mean sea-level pressure between mid (40°S) and

Deleted: by

69 high latitudes (65°S). The SAM in turn modulates the strength and position of the southern
70 westerly winds (SWW) over decadal to multi-centennial timescales, which exert a large control on
71 the synoptic scale hydrologic and heat budget (Garreaud et al., 2013). During the LGM and last
72 deglaciation, paleoclimate data indicates that the position, strength, and extent of the SWW varied
73 latitudinally, migrating southward during warmer intervals and northward during cooler intervals,
74 ultimately altering overall ice sheet mass balance (Mercer, 1972; Denton et al., 1999; Lamy et al.,
75 2010; Kilian and Lamy, 2012; Boex et al., 2013). Terrestrial paleoclimate proxies that indicate
76 that the CLD was wetter during the LGM and early deglaciation have been used to support the
77 idea that the SWW migrated northward of 41°S across the CLD (Moreno et al., 1999; Moreno et
78 al., 2015; Moreno and Videla, 2018; Diaz et al., 2023). Additionally, these proxies indicate a
79 switch from hyper humid to humid conditions around 17,300 cal yr BP, which was inferred by
80 Moreno et al. (2015) to indicate the poleward migration of the SWW south of the CLD.

81
82 However, inferring changes in the SWW across the last deglaciation from paleoclimate proxies
83 can be problematic as outlined by Kohfeld et al. (2013) who compiled an extensive dataset of
84 paleoclimate archives that record changes in moisture, precipitation-evaporation balance, ice
85 accumulation, runoff and precipitation, dust deposition, and marine indicators of sea surface
86 temperature, ocean fronts, and biologic productivity. Kohfeld et al. (2013) conclude that
87 environmental changes inferred from existing paleoclimate data could be potentially explained by
88 a range of plausible scenarios for the state and change of the SWW during the LGM and last
89 deglaciation, such as a strengthening, poleward or equatorward migration, or no change. Climate
90 model results from Sime et al. (2013) indicate that the reconstructed changes in moisture from
91 Kohfeld et al. (2013) can be simulated well without invoking large shifts or changes in strength to
92 the SWW. This discrepancy also exists amongst climate models which diverge on whether the
93 LGM SWW was shifted equatorward or poleward, and was stronger or weaker than present day
94 (Togweiler et al., 2006; Menviel et al., 2008; Rojas et al., 2009; Rojas et al., 2013; Sime et al.,
95 2013; Jiang et al., 2020). Therefore, from paleoclimate proxies and climate models, we still do
96 not have a firm understanding of how the SWW may have changed during the last deglaciation,
97 and how these variations may have influenced the deglaciation of the PIS.

98
99 Early paleo ice sheet modelling experiments across the PIS have focused on evaluating the
100 relationship between the simulated LGM ice sheet geometry in response to spatially uniform
101 temperature change (Hulton et al., 2002; Sugden et al., 2002; Hubbard et al., 2005). While these
102 early simulations provided constraints on PIS areal extent, ice volume, and sensitivity to LGM
103 temperature depressions, spatially varying temperature and precipitation were not considered.
104 Recently, Yan et al. (2022) simulated the PIS behavior at the LGM using an ensemble of climate
105 model output from the Paleoclimate Modelling Intercomparison Project (PMIP4; Kageyama et al.,
106 2021). Results best matching the empirical reconstructions from PATICE (Davies et al., 2020)
107 suggest that reduction in temperature was likely the main driver of PIS LGM extent, although the
108 authors found that variation in regional LGM precipitation anomaly can have large impacts on the
109 simulated ice sheet geometry. This evidence is supported by recent glacier modelling across the
110 northeastern Patagonian Andes which suggests that increases in precipitation during the
111 termination of the LGM are necessary to achieve modeled fit with reconstructed glacier extent
112 (Muir et al., 2023; Leger et al., 2021b). Additionally, Martin et al. (2022) found that precipitation
113 greater than present day is needed to explain late glacial and Holocene ice readvance of the Monte
114 San Lorenzo ice cap, lying to the southeast of the current Northern Patagonian Ice Field. These

Deleted: ,

Deleted:

Deleted: are

118 regional studies therefore provide further evidence that late glacial and deglacial variability in
119 precipitation, perhaps driven by changes in the SWW, influenced PIS retreat and readvance over
120 numerous timescales.

121
122 To advance our understanding of the last glacial and deglacial ice behavior across the CLD, we
123 use a numerical ice sheet model to simulate the LGM ice geometry and deglacial ice retreat using
124 transiently evolving boundary conditions from a climate model simulation of the last 21,000 years
125 (TraCE-21ka; Liu et al., 2009; He et al., 2013) which simulates large scale variability in the
126 strength and position of the SWW (Jiang and Yan, 2020). Because there is a lack of transiently
127 evolving ice sheet model simulations of the PIS across the last deglaciation, our aim is to provide
128 possible constraints on the nature of ice retreat across the CLD region, from which the
129 reconstructions (PATICE; Davies et al., 2020) are uncertain. Also, by assessing the sensitivity of
130 our ice sheet experiments to a range of climatic boundary conditions, we aim to provide additional
131 insight into the dominant climatic controls on the deglacial evolution of the PIS in the CLD region.

132

133 **2 Methods: Model description and setup**

134

135 **2.1 Ice sheet model**

136

137 In order to simulate the ice margin migration across the CLD during the LGM and last deglaciation,
138 we use the Ice Sheet and Sea-level System Model (ISSM), a thermomechanical finite-element ice
139 sheet model (Larour et al., 2012). Because of the high topographic relief across the CLD and
140 associated impact on ice flow, we use a higher-order approximation to solve the momentum
141 balance equations (Dias dos Santos et al., 2022). This ice flow approximation is a depth-integrated
142 formulation of the higher-order approximation of Blatter (1995) and Pattyn (2003), which allows
143 for an improved representation of ice flow compared with more traditional approaches in paleo-
144 ice flow modelling (e.g., Shallow Ice Approximation or hybrid approaches; Hubbard et al., 2005;
145 Leger et al., 2021b; Yan et al., 2022), while allowing for reasonable computational efficiency. Our
146 model domain comprises the northernmost LGM extent of the PIS across the CLD, extending
147 beyond the LGM ice extent reconstructed from Davies et al. (2020) and ends along the northern
148 shore of the Golfo de Ancud (Figure 2).

149

150 We rely on anisotropic mesh adaptation to create a non-uniform model mesh that varies based
151 upon gradients in bedrock topography from the General Bathymetric Chart of the Oceans
152 (GEBCO; GEBCO Bathymetric Compilation Group, 2021), a terrain model for ocean and land.
153 For the land component, the GEBCO model uses version 2.2 of the Surface Radar Topography
154 Mission data (SRTM15_plus; Tozer et al., 2019), to create a 15 arc second gridded output of terrain
155 elevation relative to sea level. Our ice sheet model horizontal mesh resolution varies from 3 km
156 in areas of low bedrock relief to 450 meters in areas where gradients in the bedrock topography is
157 high and comprises 40,000 model elements. We impose no boundary conditions of ice flow and
158 thickness at the southern extent of our model domain. Due to the north-south nature of the
159 simulated ice divide during the last deglaciation (see Figure 4), inflow from the south and into our
160 model domain is minimal and was found to not impact our results. ▼

161

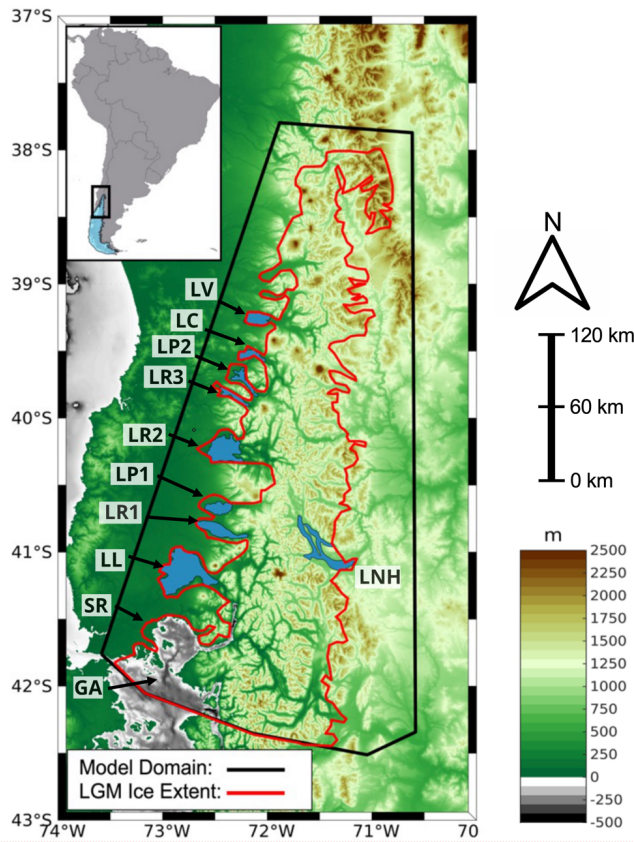
162

163

Deleted: 2

Deleted:

166
167
168
169
170
171
172
173
174
175
176
177
178
179
180
181
182
183
184
185
186
187
188
189
190
191
192
193
194
195
196



Commented [JC1]: Added Scale Bar and North Arrow.

197
198
199
200
201
202
203
204

Although geomorphological evidence suggests that while southernmost glaciers across the PIS may have been temperate with warm based conditions during the LGM, there may have been periods where ice lobes were polythermal (Darvill et al., 2016). However, recent ice flow modelling (Leger et al., 2021b) suggests that varying ice viscosity mainly impacts the accumulation zone thickness in simulations of paleoglaciers in Northeastern Patagonia, with minimal impacts on overall glacier length and extent. Accordingly, based on sensitivity tests (see supplement section S1), our model is 2-dimensional and we do not solve for ice temperature and viscosity allowing for increased computational efficiency. For our purposes, we use Glen's flow

Deleted: <object>

206 law (Glen, 1955) and set the ice viscosity following the rate factors in Cuffey and Paterson (2010)
207 assuming an ice temperature of -0.2°C . We use a linear friction law (Budd et al., 1979)

$$209 \tau_b = -k^2 N \mathbf{u}_b \quad (1)$$

210 where τ_b represents the basal stress, N represents the effective pressure, and \mathbf{u}_b is the magnitude
211 of the basal velocity. Here $N = g(\rho_i H + \rho_w Z_b)$, where g is gravity, H is ice thickness, ρ_i is the
212 density of ice, ρ_w is the density of water, and Z_b is bedrock elevation following Cuffey and Paterson
213 (2010).
214

215 The spatially varying friction coefficient, k , is constructed following Åkesson et al. (2018):
216

$$217 k = 200 \times \frac{\min[\max(0, z_b + 600), z_b]}{\max(z_b)} \quad (2)$$

218 where z_b is the height of the bedrock with respect to sea level. Using this parameterization, basal
219 friction is larger across high topographic relief and lower across valleys, and areas below sea level.
220

221 To account for the influence of glacial isostatic adjustment (GIA), we prescribe a transiently
222 evolving reconstruction of relative sea level from the global GIA model of the last glacial cycle
223 from Caron et al. (2018). This includes three physical components: 1) Bedrock vertical motion
224 2.) Eustatic sea level, and 3.) Geoid changes. The time series we use to prescribe GIA is from the
225 model average of an ensemble of GIA forward model estimations from Caron et al., 2018. The
226 prescribed GIA is in good agreement (Figure S2) with a reconstruction of relative sea-level change
227 from an isolation basin in central Patagonia (Troch et al., 2022). This methodology has been
228 applied in recent modelling following Cuzzone et al. (2019) and Briner et al. (2020).
229

230 2.2 Experimental Design

231 In order to simulate the ice history at the LGM and across the last deglaciation we use climate
232 model output from the National Center for Atmospheric Research Community Climate System
233 Model (CCSM3) TraCE-21ka transient climate simulation of the last deglaciation (Liu et al., 2009;
234 He et al., 2013). Monthly mean output of temperature and precipitation are used from these
235 simulations as inputs to our glaciological model (full climate forcings details are further described
236 in section 2.4) and we use the monthly mean output every 50 years across the last deglaciation.
237 Large, multi-proxy reconstructions from He and Clark (2022), Liu et al. (2009), He et al. (2011),
238 and Shakun et al. (2012; 2015) have all demonstrated good agreement between TRACE 21k and
239 a wide variety of paleo-proxy data during the last deglaciation that include records from the West
240 Antarctic and South America.
241

242 2.3 Surface Mass Balance

243 In order to simulate the deglaciation of the PIS across our model domain we require inputs of
244 temperature and precipitation to estimate the surface mass balance. To derive snow and ice melt
245 we use a positive degree day model (Tarasov and Peltier, 1999; Le Morzadec et al., 2015; Cuzzone
246 et al., 2019; Briner et al., 2020). Our degree day factor for snow melt is $3 \text{ mm } ^{\circ}\text{C}^{-1}\text{day}^{-1}$ and 6 mm
247 $^{\circ}\text{C}^{-1}\text{day}^{-1}$ for bare ice melt, and we use a lapse rate of $6 \text{ }^{\circ}\text{C}/\text{km}$ to adjust the temperature of the
248

249 climate forcings to surface elevation, which are within a range of typical values used to model
 250 contemporary and paleo glaciers across Patagonia (see Fernandez et al., 2016 Table 3; Yan et al.,
 251 2022). The hourly temperatures are assumed to have a normal distribution, of standard
 252 deviation 3.5 degrees Celsius around the monthly mean. An elevation-dependent desertification
 253 is included (Budd and Smith, 1981) which reduces precipitation by a factor of 2 for every kilometer
 254 change in ice sheet surface elevation. We note that the values in the surface mass balance
 255 parameters were chosen to provide a reasonable fit within 5% between the simulated LGM ice
 256 sheet area and the reconstructed ice area from PATICE (see Figure 4 and 10).

2.4 Climate forcings

258
 259
 260 In order to scale monthly temperature and precipitation across the LGM and last deglaciation we
 261 applied a commonly used modeling approach (Pollard et al., 2012; Seguinot et al., 2016; Golledge
 262 et al., 2017; Tigchelaar et al., 2019; Clark et al., 2020; Briner et al., 2020; Cuzzone et al., 2022; Yan

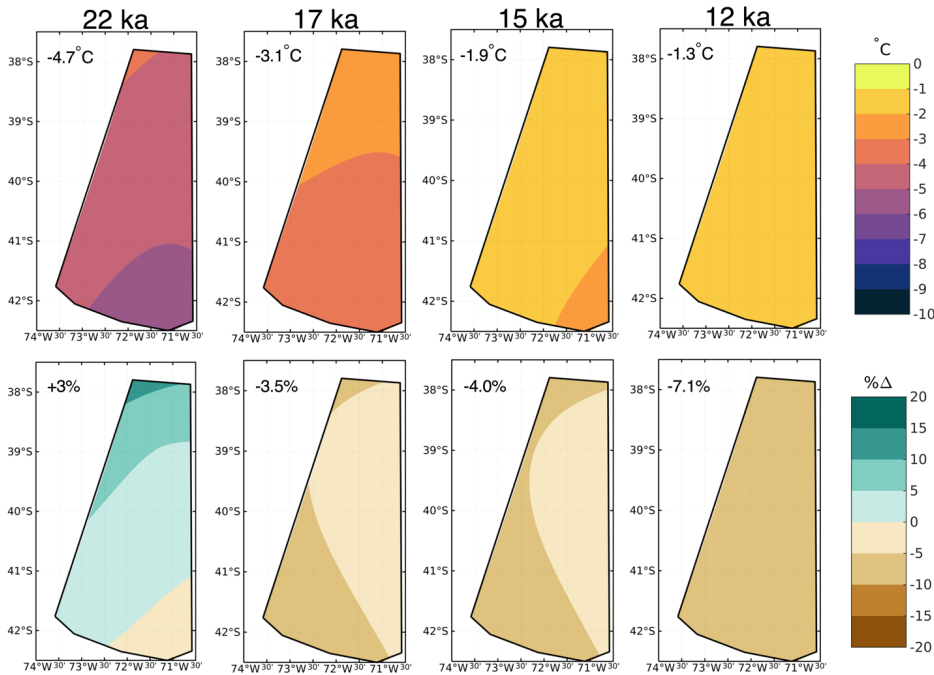


Figure 3. The bilinearly summer (DJF) temperature (top row) and winter (JJA) precipitation anomalies (bottom row) from TraCE-21ka at 22 ka, 17 ka, 16 ka, and 12 ka. Anomalies are taken as the difference between the corresponding time period and preindustrial (LGM-PI), with the precipitation anomalies expressed as the percent difference from preindustrial. The area averaged value of the anomaly is shown in the upper left corner of each

263 et al., 2022; equations 3 and 4). First, we use the monthly mean climatology of temperature and
 264 precipitation for the period 1979-2018 ($T_{(1979-2018)}, P_{(1979-2018)}$) from the Center for Climate
 265

Deleted:

Deleted:

Deleted: LGM

Deleted: anomalies

Deleted: y

Deleted: l

Deleted: eft panel

Deleted: the

Deleted: LGM

Deleted: y

Deleted: right panel)

Deleted: LGM

Deleted: of the LGM

268 Resilience Research Meteorological dataset version 2.0 (CR2MET; Boisier et al., 2018). This
 269 output, which uses information from a climate reanalysis and is calibrated against rain-gauge
 270 observations, is provided at 5 km spatial resolution.

271 We then bilinearly interpolate these fields onto our model mesh.

$$274 T_t = T_{(1979-2018)} + \Delta T_t \quad (3)$$

$$276 P_t = P_{(1979-2018)} + \Delta P_t \quad (4)$$

277 Next, anomalies of the monthly temperature and precipitation fields from TraCE-21ka (Liu et al.,
 278 2009; He et al., 2013) are computed as the difference from the preindustrial control run and
 279 interpolated onto our model mesh (ΔT_t and ΔP_t). These anomalies are added to the contemporary
 280 monthly mean as shown in equations 3 and 4, to produce the monthly temperature and precipitation
 281 fields at LGM and across the last deglaciation (T_t and P_t). In Figure 3 anomalies from preindustrial
 282 of summer temperature and winter precipitation are shown for 22 ka, 17 ka, 15 ka, and 12 ka.

285 2.5 Ice front migration and iceberg calving

287 We simulate calving where the PIS interacts with ocean, but do not include any treatment of
 288 calving in proglacial lakes (see section 4.3). We track the motion of the ice front using the level-
 289 set method described in Bondzio et al. (2016; equation 3) in which the ice velocity \mathbf{v}_f is a function
 290 of the ice velocity vector at the ice front (\mathbf{v}), the calving rate (c), the melting rate at the calving
 291 front (M), and where \mathbf{n} is the unit normal vector pointing horizontally outward from the calving
 292 front. For these simulations the melting rate is assumed to be negligible compared to the calving
 293 rate, so M is set to 0.

$$295 \mathbf{v}_f = \mathbf{v} - (c + M) \mathbf{n} \quad (5)$$

297 To simulate calving we employ the more physically based Von Mises stress calving approach
 298 (Morlighem et al., 2016) which relates the calving rate (c) to the tensile stresses simulated within
 299 the ice, where σ is the von Mises tensile strength, $\|\mathbf{v}\|$ is the magnitude of the horizontal ice
 300 velocity, and σ_{max} is the maximum stress threshold which has separate values for tidewater and
 301 floating ice, namely 1 MPa and 200 kPa.

$$303 c = \|\mathbf{v}\| \frac{\sigma}{\sigma_{max}} \quad (6)$$

305 The ice front will retreat if von Mises tensile strength exceeds the user defined stress threshold.
 306 This calving law has been applied in Greenland to assess marine terminating icefront stability
 307 (Bondzio et al., 2016; Morlighem et al., 2016; Choi et al., 2021; Cuzzone et al., 2022) and for our
 308 simulations applies where ocean is present such as the Seno de Reloncaví and the Golfo de Ancud
 309 (see Figure 2).

311 3 Results

312

Deleted: ¶

Deleted: ¶

Deleted:

Deleted: we show the

Deleted: of

Deleted:

Formatted: Font:

Deleted: ¶

Deleted: (v_f)

Deleted:)

Deleted: v

Deleted: v

Deleted: c

Deleted: n

Deleted: To simulate calving we employ the more physically based Von Mises stress calving approach (Morlighem et al., 2016) which relates the calving rate (c) to the tensile stresses simulated within the ice, where σ is the von Mises tensile strength, $\|\mathbf{v}\|$ is the magnitude of the horizontal ice velocity, and σ_{max} is the maximum stress threshold which has separate values for grounded and floating ice. ¶

Deleted: c

Deleted: v

Deleted: The ice front will retreat if von Mises tensile strength exceeds a user defined stress threshold, which we set to 200 kPa for floating ice and 1 MPa for tidewater ice. This calving law has been applied in Greenland to assess marine terminating icefront stability (Bondzio et al., 2016; Morlighem et al., 2016; Choi et al., 2021; Cuzzone et al., 2022) and for our simulations applies where ocean is present such as the Seno de Reloncaví and the Golfo de Ancud (see Figure 2). ¶

344 **3.1 Simulated LGM state**

345
346 In order to arrive at a steady state LGM ice geometry, we first initialize our model with an ice-free
347 configuration. A constant LGM monthly climatology of temperature and precipitation are then
348 applied, as well as the prescribed GIA from Caron et al. (2018). We allow the ice sheet to relax for
349 10,000 years, during which, the ice sheet is free to grow and expand until it reaches a steady state
350 ice geometry and volume, in equilibrium with the climate forcings.

351
352 At 22 ka, Trace-21ka simulates an area averaged summertime (DJF) cooling of 4.7°C relative to
353 the PI across our model domain (Figure 3). The LGM cooling increases from north to south, with
354 the greatest magnitude of cooling occurring across the southern portion of our model domain of
355 up to 6°C. During winter (JJA), Trace-21ka simulates an overall wetter climate across our model
356 domain during the LGM relative to the PI. While the area-averaged LGM precipitation anomaly
357 is small (3% higher), the LGM precipitation anomaly increases from south to north, with Trace-
358 21ka simulating 10-15% more wintertime precipitation during the LGM than the PI across the
359 northern portion of the model domain.

Deleted: <object>

Deleted: While the mean position of the wintertime SWW is simulated to be poleward during the LGM relative to the PI in TraCE-21ka (Jiang and Yan, 2022), the low-level zonal wind (925 hPa) is stronger during the LGM across our model domain and Patagonia (Figure S3A). We also find that relative to PI, wintertime low level (850 hPa) moisture flux convergence is higher during the LGM across our model domain (Figure S4A).

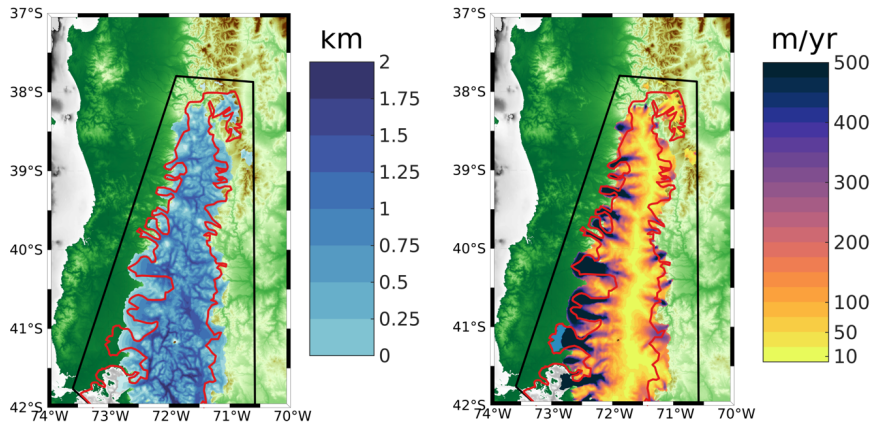


Figure 4. The simulated LGM ice thickness (km; left panel) and the simulated LGM ice surface velocity (km/yr; right panel) is shown. The black outline denotes our ice sheet model boundary, and the red line denotes the LGM reconstructed ice extent from PATICE (Davies et al., 2020).

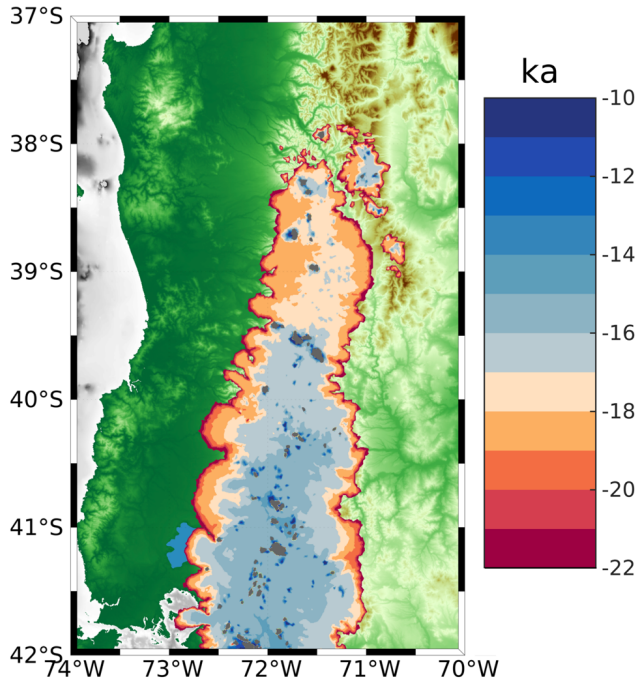
361 Bedrock elevation increases from west to east, with deep valleys interspersed across most of our
362 model domain (Figure 2). LGM ice thickness is greatest in these valleys (upwards of 2000 meters)
363 where driving stresses dominate and where bedrock geometry controls the flow of ice from higher
364 terrain and through these valleys (Figure 4). Across the highest terrain such as the many volcanoes
365 across the CLD, ice is comparatively thinner than the surrounding valleys. An ice divide is present
366 as slow ice velocities in the interior of the ice sheet, which give way to fast flowing outlet glaciers
367 especially on the western margin of the CLD where velocities reach in excess of 500 m/yr and in
368 some location up to 2 km/yr. The simulated LGM ice sheet area across the CLD is 414,120 km²,

378 which is within 1% of the area calculated from the PATICE reconstruction (414,690 km²; [Figure](#)
379 [10](#)). This agreement is in part due to the tuning of our degree day factors as discussed in section
380 2.3, and gives confidence to our ability to simulate a reasonable LGM ice sheet across the CLD
381 and throughout the last deglaciation.
382

383 3.2 Simulation of the Last Deglaciation

384
385 Monthly mean temperature and precipitation, taken every 50 years from the TraCE-21ka (Liu et
386 al., 2009; He et al., 2013) experiment is used to drive our simulation of ice history across the last
387 deglaciation (22 ka – 10 ka). The transient simulation is initialized with the LGM ice sheet
388 geometry shown in Figure 4, and is run forward with the appropriate climate boundary conditions
389 until 10 ka.

391 3.2.1 Pattern of Deglaciation



418
419 Figure 5. The simulated deglaciation age for the transient simulation from the LGM to 10 ka. The gray color
420 indicates where ice persists after 10 ka.

421 From the resulting transient simulation, we calculate the timing of deglaciation across our model
422 domain (Figure 5) as the youngest age at which grid points become ice free. Our map of the

Deleted:). Because of possible readvances during the deglaciation, we select

425 simulated deglaciation can be paired with a timeseries of the rate of ice mass change (Figure 6) to
426 highlight some key features in the magnitude and timing of ice retreat between 22 ka and 10 ka.

427
428 Between 22 ka to 19 ka, the ice sheet undergoes periods of minor to moderate ice mass loss and
429 gain in an interval of time where summer temperature anomalies (Figure 6) and the corresponding
430 ice margin remain relatively stable (Figure 5). Between 19 ka and 18.5 ka, coincident with a rise
431 in summertime temperature (Figure 6), a pulse of ice mass loss exceeding 5,000 GT/century occurs
432 before trending toward minimal ice mass loss around 18 ka as the rise in summer temperature
433 levels off. During this time interval, the ice margin pulls back considerably towards higher terrain
434 across the northern portion of the model domain (Figure 5), and many of the fast-flowing outlet
435 glaciers on the western margin retreat back towards the ice sheet interior. Between 18 ka to 16.2
436 ka, summer temperature rises steadily $\sim 1.2^\circ\text{C}$ and is punctuated with an abrupt warming of $\sim 0.5^\circ\text{C}$
437 at 16 ka (Figure 6). During this interval, ice mass loss remains high and steady at ~ 1000
438 GT/century with pulses of increased mass loss at 17.8 ka, 16.8 ka, and 16 ka varying between
439 2000-5000 GT/century (Figure 6).
440

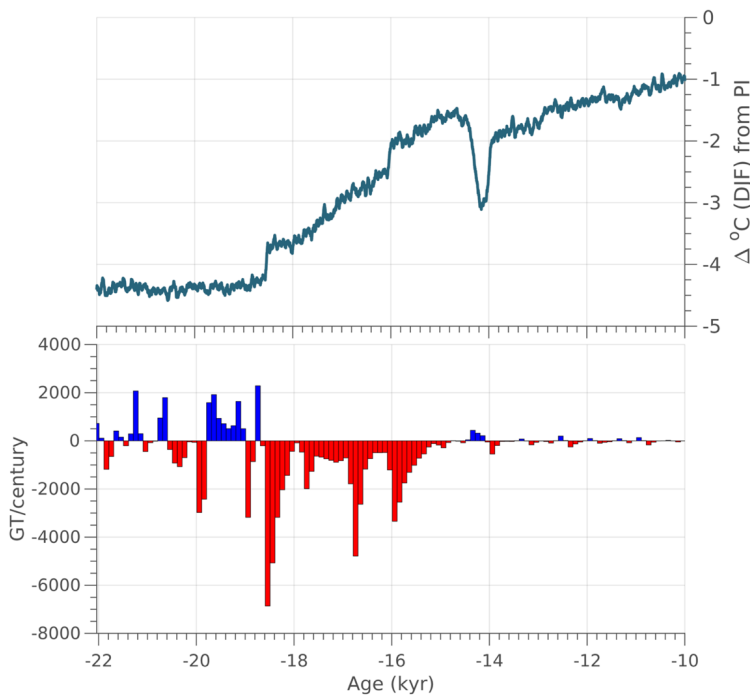


Figure 6. Top Panel: The TraCE-21ka Summer (DJF) temperature anomaly taken as the difference from the preindustrial period, area averaged across our model domain. Bottom Panel: The simulated ice mass change calculated in GT/century across the last deglaciation (22 ka to 10 ka). Red indicates ice mass loss, and blue indicates ice mass gain.

441

442 By 17 ka, the northern portion of the model domain (north of 39.5°S), has generally become ice
 443 free for the exception of the highest terrain (e.g., mountain glaciers). By 16 ka, between 39.5°S
 444 and 40.5°S, ice remains only on the highest terrain (Figure 5), however ice cover persists south of
 445 40.5°S. Between 16 ka and 15 ka, summer temperature rises ~0.5°C (Figure 6) and the remaining
 446 ice sheet retreats south of 40.5°S. By 15 ka, there is no evidence of an ice sheet, with only
 447 mountain glaciers and small ice caps (e.g. Cerro Tronador) existing across the high terrain
 448 throughout the model domain (Figure 5).

449
 450 After 15 ka, TraCE-21ka simulates a short and abrupt Antarctic Cold Reversal (ACR) between
 451 14.6 ka and 14 ka (Figure 6), before temperatures continue to rise into the early Holocene. There
 452 is only a minor ice mass gain (e.g., <500 GT/yr) during the ACR, and minimal fluctuation in ice
 453 mass after 14 ka. By 10 ka, only small mountain glaciers persist across the high terrain and
 454 volcanoes of the CLD (gray color in Figure 5).

455 3.2.2 Sensitivity Tests

456
 457 To better assess how changes in precipitation may modulate the deglaciation across the CLD we
 458 perform additional sensitivity tests. We refer to the simulation discussed above as our *main*
 459 *simulation*, where the climate boundary conditions of temperature and precipitation varied
 460 temporally and spatially across the last deglaciation. Three more simulations are performed where
 461 temperature is allowed to vary across the last deglaciation, but precipitation remains fixed at a
 462 given magnitude for a particular time interval. Each experiment is listed below as:

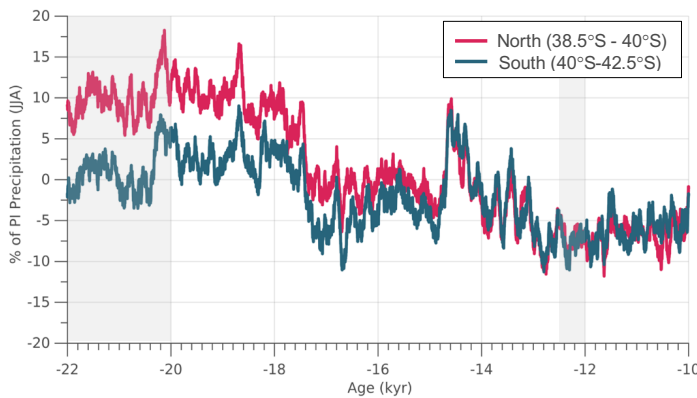


Figure 7. The winter (JJA) precipitation anomaly expressed as the percent difference from the preindustrial period. The area averaged anomaly is shown for the region north of 40°S and for the region south of 40°S (see Figure 2 for reference to the latitudinal range of our model domain). Intervals of time used in the sensitivity tests are highlighted by the gray shading.

464 Precip. PI: Monthly precipitation is held constant at the preindustrial mean. Preindustrial
 465 precipitation is reduced compared to the period 22 ka to 18 ka, but is similar to and higher than
 466 what is simulated after 18 ka for the exception of the ACR at 14.5 ka (Figure 7).

Commented [JC2]: Note, we changed the color of the legend line in Figure 7. North and South is now the correct color in the legend. This was not corrected in the last revision.

- Deleted:
- Formatted: Font: Italic
- Formatted: Font color: Text 1
- Formatted: Font: Italic
- Formatted: Font color: Text 1
- Formatted: Normal, Indent: Left: 0.25", No bullets or numbering

467 *Precip. 12 ka*: Monthly precipitation is held constant at the 12.5 ka-12 ka mean. This is a
468 period of reduced precipitation relative to the preindustrial (~7% reduction; Figure 7).

469 *Precip LGM*: Monthly precipitation is held constant to the 22-20 ka mean, which is
470 approximately 10% higher than preindustrial values across the Northern portion of the model
471 domain (North of 40°S).

472 Across our model domain during experiment *Precip. PI* (Figure 8A), wintertime precipitation
473 during the preindustrial is reduced compared to the early deglaciation (22 ka to 18ka) and is similar
474 to slightly higher particularly south of 40°S after 18 ka (Figure 7). When holding precipitation
475 constant at the preindustrial mean through the last deglaciation, the ice retreats faster across most
476 portions of the model domain, particularly along the ice margins and in area north of 40°S. In the
477 southern portion of our model domain (south of 40°S), where the changes in deglacial precipitation
478 relative to the preindustrial are lower (Figure 3 and 7), the difference in simulated deglaciation age
479 are also smaller. In general, the pace of deglaciation increases by up to 1 kyr compared to the
480 main simulation, with many locations experiencing deglaciation 200-600 yrs earlier than the main
481 simulation.

482

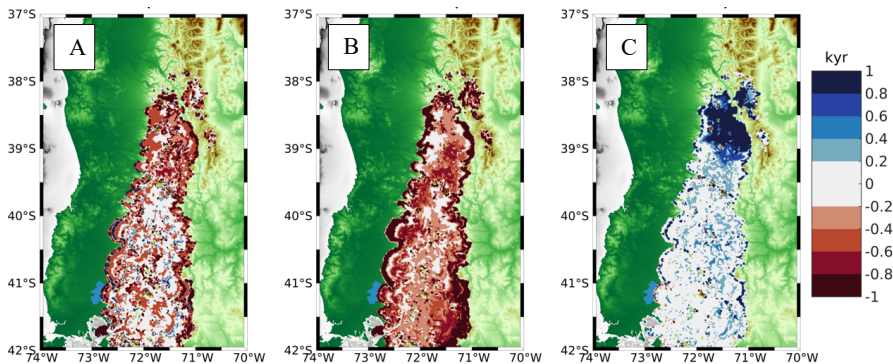


Figure 8. A) The difference in the simulated deglaciation age between sensitivity experiment *Precip. PI*; B.) experiment *Precip. 12 ka*; C.) and experiment *Precip LGM*, from the main simulation. Blue colors indicate slower ice retreat for the sensitivity experiments compared to the main simulation, while red colors indicate faster ice retreat for the sensitivity experiments compared to the main run.

483 For experiment *Precip. 12 ka*, winter precipitation is reduced by up to 7% (Figure 8B) relative to
484 the preindustrial across the model domain (Figure 3 and 7). In this experiment ice retreats faster
485 across most of the CLD, from the ice margins and through the interior. Deglaciation along the
486 margins occurs >1 kyr faster in many locations, and between 200 yrs to 1 kyr faster across portions
487 of the ice interior. For experiment *Precip LGM*, winter precipitation is increased by up to 10%
488 (Figure 8C; *Precip LGM*): across the northern portion of the model domain (north of 40°S) relative
489 to preindustrial, but is similar to preindustrial values across the southern portion of our model
490 domain (south of 40°S). In this experiment, with the imposed higher precipitation across the

Formatted: Font: Italic

Formatted: Font color: Text 1

Formatted: Font: Italic

Formatted: Font color: Text 1

Formatted: Font: Italic

Formatted: Font color: Text 1

Formatted: Font color: Text 1

Deleted: ¶
<object>Monthly precipitation is held constant to the 22-20 ka mean, which is approximately 10% higher than preindustrial values across the Northern portion of the model domain (North of 40°S).¶

Deleted: 2

Deleted:

Deleted:

Deleted: 7

Deleted: 7

Deleted: 2

Deleted: 3

Deleted: 4

Deleted: our other two sensitivity tests

Deleted: ; *Precip. 12 ka*

Moved (insertion) [1]

Deleted: 7

Deleted: along

Deleted:

Deleted: and

Moved up [1]: ice retreats faster across most of the CLD, along the ice margins and through the interior. Deglaciation along the margins occurs >1 kyr faster in many locations, and between 200 yrs to 1 kyr faster across portions of the ice interior. In

Deleted: For experiment *Precip. 12 ka*

Deleted: 2

Deleted: *Precip LGM*

Deleted: 3

Deleted:

517 northern portion of the model domain, ice retreats slower during the last deglaciation relative to
518 our standard simulation by >1 kyr, and in some locations up to 2 kyr.

519 3.3 Comparison to the reconstructed deglacial ice extent

520 Shown in Figure 1, PATICE assigns high to medium confidence to the reconstructed LGM (25 ka
521 – 20 ka) ice extent along most of the western ice margin and portions of the eastern margin, with
522 low confidence assigned to the northernmost ice extent. The majority of the ice history is poorly
523 constrained (low confidence) during the deglaciation, and PATICE reconstructs a small cap that
524 persists across the southern CLD until 10 ka, after which the ice disappears and only the Cerro

Deleted: ¶

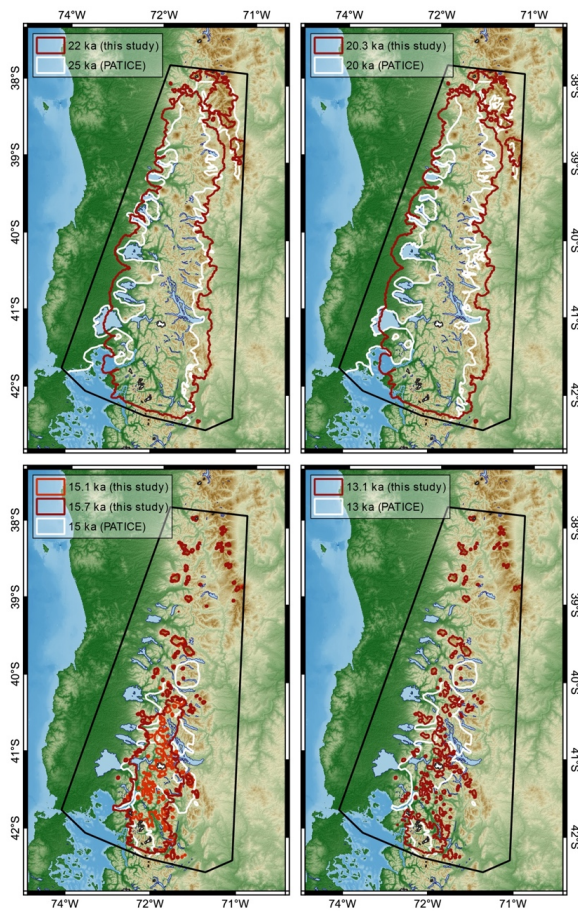


Figure 9. Comparison between the simulated ice extent at time intervals closest to the corresponding reconstructed ice extent from PATICE (Davies et al., 2020).

526 Tronador glacier remains (see Figure 13 from Davies et al., 2020). We show the simulated and
527 reconstructed ice extent in Figure 9 as well as the calculated ice area from PATICE at 20 ka, 15
528 ka, 13 ka, and 10ka and for our transient simulation in Figure 10. At 22 ka (Figure 9), our model
529 simulates a generally greater ice extent along the eastern and western margin, except at the Seno
530 de Reloncaví, Golfo de Ancud, and Lago Llanquihue, where the simulated ice margin does not
531 advance to the well dated terminal LGM moraines (Mercer, 1972; Porter, 1981; Andersen et al.,
532 1999; Denton et al., 1999). At 20 ka, the simulated ice area is $4.1 \times 10^4 \text{ km}^2$ which is nearly identical
533 to the PATICE areal extent across our model domain (Figure 10). The ice margin at the Seno de
534 Reloncaví, Lago Llanquihue, and other locations along the eastern boundary in the CLD advances
535 slightly at 20 ka, but still remain inboard of the PATICE reconstruction for these regions.

536
537 Between 18.3 ka and 15 ka large scale ice retreat occurs, and the simulated ice sheet loses 90% of
538 its ice area, while the PATICE reconstruction suggests a reduction of 75% (Figure 10). At 15 ka,
539 PATICE reconstructs an existing ice cap that separates from the remainder of the PIS to the south
540 (Figure 9). This is in contrast to the simulated ice extent, which shows that by 15 ka, the PIS
541 across our model domain has completely retreated and only mountain glaciers or small ice caps
542 exist amongst the high terrain. However, if we compare the PATICE area at 15 ka and the
543 simulated ice area at 15.7 ka (Figure 10; [green rectangle](#)), they are nearly identical at $1.2 \times 10^4 \text{ km}^2$.
544 While the PATICE ice extent at 15 ka and the simulated ice extent 15.7 ka do not match
545 completely, the simulated ice extent at 15.7 ka still has evidence of a large ice cap similar to the
546 PATICE reconstruction. Therefore, the simulated transition from ice sheet to ice cap and to
547 discrete mountain glaciers occurs between 15.7 ka and 15 ka in our simulations. By 13 ka, our
548 simulated ice area is 60% lower than the PATICE reconstructed area. By 10 ka this difference is
549 50%, however by this time the majority of the ice sheet has deglaciated (Figure 10), with our model
550 simulating discrete mountain glaciers while PATICE reconstructs a small and narrow ice cap
551 across the high terrain in the southern CLD (also see Figure 1).

552
553

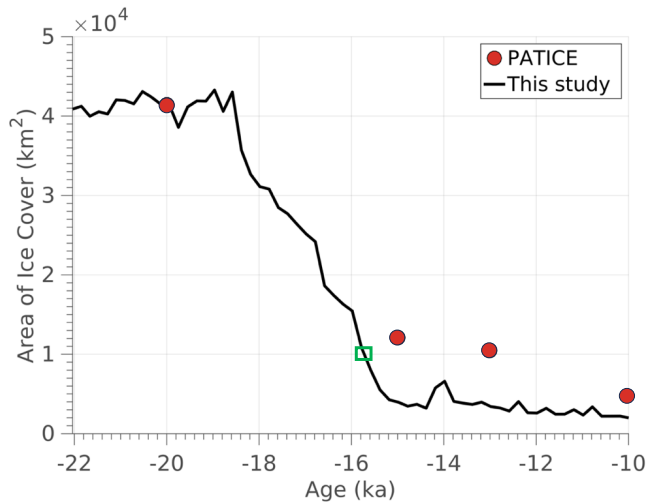


Figure 10. The simulated ice area (km²) from 22 ka to 10 ka shown as the black line. The red dots indicate the calculated ice area across our model domain for the reconstructed ice extent from PATICE (Davies et al., 2020). The green rectangle highlights the simulated ice area at 15.7 ka.

555

556 4 Discussion

557

558 4.1 Climate-ice sensitivity

559

560 Determining the influence of the SWW on the heat and hydrologic budget across South America
 561 during the LGM and last deglaciation remains difficult, as paleo-proxy data is limited and climate
 562 models tend to disagree on the evolution of the SWW (Kohfeld, 2013; Berman et al., 2018). And
 563 while paleo-proxy evidence does suggest wetter conditions across the CLD during the late glacial
 564 (Moreno and Videla, 2018), linking this variability to changes in the position and strength of the
 565 SWW remains difficult (Kohfeld et al., 2013).

566

567 The scale at which we deduce ice history and climate interactions is also important. Looking at
 568 the PIS as a whole, recent numerical ice sheet modelling studies indicate that the simulated ice
 569 extent and volume for the entire PIS at the LGM is largely controlled by the magnitude of the
 570 temperature anomaly compared to present day (Yan et al., 2022). However, regional scale ice
 571 flow modelling informed by geologic constraints on past ice margin extent show that higher
 572 precipitation during the LGM (Leger et al., 2021b), the late glacial, and the Holocene (Muir et al.,
 573 2023; Martin et al., 2022) is needed to support model-data agreement. It appears that during the
 574 LGM a northward shift in the SWW (Kohfeld et al., 2013; Rojas et al., 2009; Togweillier et al.,
 575 2006) or a strengthening or expansion of the wind belt (Lamy et al., 2010) is perhaps the most
 576 likely scenario, with high frequency variability possible during the deglaciation as atmospheric
 577 reorganization altered the heat and hydrologic budget as recorded by glacier and ice sheet change
 578 (Davies et al., 2020; Boex et al., 2013).

Deleted: limitations in

Deleted: disagreement between

Deleted: prohibit certainty

Deleted: the paleoclimate

Deleted:

Deleted: SWW

Deleted: and

Deleted: from regional paleoclimate proxies

Deleted: problematic

588 We analyzed outputs of the wintertime (JJA) 925 hPa zonal wind as the mean over 500 yr periods
589 from TraCE-21ka for the LGM (22-21ka), 18ka (18.5-18ka), 16ka (16.5-16ka), 14ka (14.5-14ka),
590 12ka (12.5-12ka) and the Preindustrial (Supplemental section 3, Figures S3 A-E). Across our
591 model domain and to its south, relative to the PI, zonal winds are stronger during the LGM with a
592 southerly displacement (Figure S3A first and second column). During 18ka (Figure S3B), the zonal
593 wind increases in strength relative to the PI, with the stronger winds having wider latitudinal
594 coverage, particularly across our model domain. While the mean position of the SWW is poleward
595 at 18ka relative to the PI (Jiang and Yan, 2022), across Patagonia the simulated position of the
596 maximum zonal wind is at the same latitudinal band as the PI. At 16ka, the zonal wind is stronger
597 across our domain and Patagonia (Figure S3C) relative to the PI, although not as large as the
598 differences during 18ka. By 14ka, the strength in the zonal winds across Patagonia and our model
599 domain are similar to slightly stronger than the PI (Figure S3D), however, the zonal wind
600 maximum is situated more equatorward across our model domain relative to the PI. By 12ka
601 (Figure S3E), the zonal wind is similar to slightly weaker than the PI across our model domain,
602 although it is stronger relative to the PI to the south of our model domain across central and
603 southern Patagonia. The position of the maximum zonal winds is also displaced further south
604 relative to the PI. These changes in strength and position of the simulated SWW during the last
605 deglaciation are similar to the findings of Jian and Yan (2020), which found that relative to the
606 Preindustrial (PI), TraCE-21ka simulates a more poleward subtropical and subpolar jet over the
607 Southern hemisphere at the LGM. During the remainder of the LGM and last deglaciation, the
608 overall position of the SWW migrates northward in TraCE-21ka, with poleward displacements
609 during Heinrich Stadial 1 (HS1), equatorward displacements during the Antarctic Cold Reversal
610 (ACR), and poleward displacements during the Younger Dryas (YD), similar to our analysis.

611
612 Additionally, we evaluated the wintertime (JJA) low-level (850 hPa) moisture flux convergence
613 from TraCE-21ka (MFC; Supplement section 4, Figure S4A-E), which is influenced by the mean
614 flow and transient eddies in the extratropical hydrologic cycle (Peixoto and Oort, 1992). During
615 the LGM and 18 ka, MFC increases across our model domain, consistent with a convergence of
616 the mean flow moisture fields relative to the PI (Figure S4 A, B). During the LGM and 18ka, we
617 note that TraCE-21ka simulates higher JJA precipitation anomalies (relative to the PI) across our
618 model domain (Figure 7). While our analysis cannot directly constrain the source of the positive
619 precipitation anomalies (e.g., mean flow, storms), the strength of the simulated SWW in TraCE-
620 21ka increases across our model domain (Figure S3 A, B) coincident with the increases in MFC,
621 which may contribute to the positive precipitation anomalies at these time intervals (Figure 7). By
622 16ka, there is increased divergence in the 925 hPa winds and moisture relative to the PI (Figure
623 S4 C). Decreased MFC relative to the PI coincides with a reduction in precipitation across our
624 model domain that is similar to or less than the PI (Figure 7). We note that the ice thickness
625 boundary conditions used in the TraCE-21ka come from the Ice5G reconstruction (Peltier, 2004),
626 which has the PIS being completely deglaciated by 16ka. However, our analysis cannot
627 decompose whether the simulated changes in precipitation and MFC are a consequence of the
628 coupling between regional atmospheric circulation and the ice thickness boundary conditions used
629 in TraCE-21ka or if these changes represent wider interactions with changes in hemispheric
630 atmospheric circulation. By 14ka, and during the ACR, MFC increases relative to the PI (Figure
631 S4D). This is consistent with a simulated equatorward migration of the SWW as shown in Jiang
632 and Yan (2020) and our analysis (Figure S3D), and positive anomalies in precipitation across our
633 model domain relative to the PI (Figure 7). By 12ka, precipitation across our model domain is

Deleted: ¶

635 reduced relative to the PI (Figure 3 and 7), and TraCE-21ka simulates a reduction in the MFC as
636 well as a poleward migration of the SWW (Figure S3E; Jiang and Yan, 2020).

637
638 When considering proxy records of precipitation across the CLD, there is reasonable agreement
639 with the changes in precipitation simulated by TraCE-21ka. Moreno et al. (1999; 2015) and
640 Moreno and Videla (2018) find that wetter than present day conditions existed across the CLD
641 during the LGM and early deglaciation which is consistent with the precipitation anomalies
642 simulated by TraCE-21ka (Figure 3 and 7). These changes in paleoclimate proxies are attributed
643 to an intensified storm track associated with an equatorward shift of the SWW (Moreno et al. 1999;
644 2015). While TraCE-21ka instead simulates a poleward shift of the SWW during these time
645 intervals, increases in precipitation and the intensification of the storm track as inferred by Moreno
646 et al. (2015) may also be consistent with a strengthening of the SWW as simulated by TraCE-21ka
647 during these intervals (Figure S3 A, B; Rojas et al., 2009; Sime et al., 2013; Kohfeld et al., 2013).
648 Moreno et al. (2015) note that rapid warming ensues across the CLD around 17,800 cal yr BP,
649 which is similar to the timing of deglacial warming as simulated by TraCE-21ka around 18.5 ka
650 (Figure 6). Coincident with this rapid temperature rise, Moreno et al. (2015) note a shift from
651 hyper humid to humid conditions which aligns well with decreases in the simulated precipitation
652 in TraCE-21ka across our model domain (Figure 7). Lastly, Moreno et al. (1999; 2015) find that
653 colder and wetter conditions occur across the CLD during the ACR, and infer an equatorward
654 expansion of the SWW as a potential cause. While TraCE-21ka simulates an abrupt and short
655 ACR, it does simulate an equatorward expansion of the SWW (Figure S4 D; Jian and Yan, 2020),
656 associated cooling (Figure 6), and increases in precipitation (Figure 7) that agree with the proxy
657 data.

658
659 Prior numerical ice flow modelling has indicated that precipitation played an important role in
660 controlling the extent of paleoglaciers across the PIS (Muir et al., 2023; Leger et al., 2021b) by
661 modulating the pace and magnitude of ice retreat and advance during deglaciation (Martin et al.,
662 2022). Much of the TraCE-21ka simulated winter precipitation anomalies shown in Figure 3 and
663 7 are within 10% of the preindustrial value. The sensitivity tests conducted here suggest that
664 modest changes (~10%) in precipitation can alter the pace of ice retreat across the CLD on
665 timescales consistent with the resolution of geochronological proxies constraining past ice retreat.
666 We note that while TraCE-21ka simulates variations in precipitation across our model domain that
667 are consistent with hydroclimate proxies discussed above (Moreno et al., 1999; 2015; 2018), the
668 magnitude of those changes is not as large as proxy data across the CLD indicate. For example,
669 hydroclimate proxies suggest that the LGM and early deglaciation was up to 2 times wetter across
670 the CLD than present day (Moreno et al., 1999; Heusser et al., 1999). Therefore, we can deduce
671 from our sensitivity analysis here that higher precipitation anomalies during the LGM and last
672 deglaciation, forced by proposed changes in the SWW (Moreno et al., 1999; 2015), may have
673 helped offset melt from deglacial warming thereby influencing the pacing of early deglacial ice
674 retreat in this region.

675 676 **4.2 Ice retreat during the Last Deglaciation**

677
678 The PATICE dataset (Davies et al., 2020) serves as the best available reconstruction of ice margin
679 change for the PIS across the last deglaciation. This state-of-the-art compilation provides an
680 empirical reconstruction of the configuration of the PIS as isochrones every 5 ka, from 35 ka to

681 present, based on detailed geomorphological data and available geochronological evidence.
682 Because geochronological constraints on past PIS change are limited, particularly in the CLD, the
683 PATICE reconstruction assigns qualitative confidence to its reconstructed ice margins. Where
684 there is agreement between geochronological and geomorphological indicators of past ice margin
685 history (i.e., moraines), high confidence is assigned. Where geomorphological evidence suggests
686 the existence of past ice margins, but lacks a geochronological constraint, medium confidence is
687 assigned. Lastly, low confidence is assigned where there is a lack of any indicators of past ice sheet
688 extent, where the ice limits result in interpolated interpretations from immediately adjacent
689 moraines from valleys that have been mapped and dated. Across the CLD, the LGM (25 ka, 20 ka)
690 ice extent is well constrained by geologic proxies particularly in the west and southwest (Figure
691 1). The moraines that constrain the piedmont ice lobes that formed along the western boundary
692 have reasonable age control (Denton et al., 1999; Moreno et al., 1999; Lowell et al., 1995), giving
693 confidence to the LGM ice margin limits. Beyond this region, age control is sparse along the
694 western boundary for the timing of LGM ice extent, but the existence of well-defined moraines
695 along lakes in the northern CLD are assumed to be in sync with those moraines deposited to the
696 south (Denton et al., 1999). However, low confidence remains in the geologic reconstruction of
697 the LGM ice boundary along the eastern margin where little to no chronological constraints are
698 available. In general, deglaciation from the maximum LGM ice extent begins between 18 – 19 ka
699 (Davies et al., 2020), however, poor age control and a lack of geomorphic indicators make it
700 difficult to constrain the ice extent across this region during the deglaciation. For instance, a single
701 cosmogenic nuclide surface exposure date retrieved from the Nahuel Huapi moraine yielded an
702 age of ~31.4 ka (Zech et al., 2017; 41.04° S, 71.15° W). While it is assumed that the ice limit
703 behaved similarly both to the west and east, the limited existing data prevents a comprehensive
704 understanding of the ice extent at the northeastern margin. This induces the highest level of
705 uncertainty in the reconstruction and hinders our data model comparison. Therefore, we rely on
706 the PATICE dataset interpolated isochrones (low confidence) for this northeastern region as the
707 state-of-the-art reconstruction.

709 In regards to ice area and extent, our simulated ice sheet at the LGM using TraCE-21ka climate
710 boundary conditions agrees well with the PATICE reconstruction (Figure 10). Our simulations
711 reveal that deglaciation began between 19 ka to 18 ka, consistent with the Davies et al. (2020)
712 reconstruction. Notably, the simulated timing of deglaciation agrees with moraine records further
713 south on the eastern side, such as in Río Corcovado (~43° S, Leger et al., 2021a), Río Cisnes (~44°
714 S, Garcia et al., 2019), Lago Palena/General Vintter (~44° S, Soteres et al., 2022), and Río
715 Ñirehuao (~45° S, Peltier et al., 2023). On the other hand, glaciers are thought to have withdrawn
716 from their LGM position later between ~18 - 17 ka on the northwestern margin (~41° S, Denton
717 et al., 1999; Moreno et al., 2015), in the southern (~46° S, Kaplan et al., 2004), and southernmost
718 regions (~52° S, McCulloch et al., 2000; 2005; Kaplan et al., 2008; Peltier et al., 2021). The
719 simulated ice retreat continues until 15 ka, with the largest pulses in ice mass loss occurring at 18.6
720 ka, 16.8 ka, and 16 ka (Figure 6). Where PATICE estimates an ice cap around 15 ka (~40°S), our
721 simulations reveal that glaciation was restricted to high elevations. After 15 ka, mountain glaciers
722 remain in our simulation but there is no presence of a large ice cap as reconstructed in PATICE.
723 Comparison between the model simulations and PATICE becomes difficult during the 15 -13 ka
724 period as confidence in the geologic reconstruction is low due to a lack of geochronological and
725 geomorphological constraints on past ice history. Therefore, our model results offer a different
726 reconstruction to PATICE, and indicate that the ice sheet in this region largely retreated by 15 ka,

Deleted: are now presently lakes and

Formatted: Font: (Default) Times New Roman, 12 pt

Formatted: Normal (Web), Font Alignment: Baseline, Pattern: Clear (White)

Formatted: Font: (Default) Times New Roman, 12 pt

Deleted:

Deleted: Our simulations reveal that deglaciation began between 19 ka to 18 ka, consistent with the geologic proxies (Davies et al., 2020).

732 with only mountain glaciers remaining. ~~This is supported further south, where the ice sheet~~
733 ~~disintegrated at ~16 ka with paleolake draining to the Pacific Ocean (~43° S, Leger et al., 2021a)~~
734 ~~and the ice remaining limited to higher mountain areas.~~ However, during this interval, the Antarctic
735 Cold Reversal (ACR) may have influenced the heat and hydrologic budget across this region, with
736 wetter and cooler conditions interrupting the deglacial warming (Moreno et al., 2018). While
737 TraCE-21ka simulates a cooler and wetter ACR, it is short-lived, lasting about 500 years as
738 compared to 2,000 years in some ice core records or proxy-based studies (Lowry et al., 2019; He
739 et al., 2013, Pedro et al., 2015). This potential for a favorable and prolonged period of glacier
740 growth is likely missing in our simulations during the ACR.

Formatted: Font: (Default) Times New Roman, 12 pt

742 4.3 Limitations

Deleted: , which may explain some of the mismatch against the PATICE reconstruction at 15 ka – 13 ka.

Formatted: Font color: Dark Red

744 Currently ISSM is undergoing model developments to include a full treatment of solid earth-ice
745 and sea-level feedbacks (Adhikari et al., 2016). Therefore, at this time, there is no coupling
746 between the ice sheet and solid earth. Instead, we prescribed GIA from a global GIA model of the
747 last glacial cycle from Caron et al. (2018). While this model reasonably estimates GIA across the
748 PIS over the last deglaciation, our simulated ice history does not feedback onto GIA. The ice
749 history for Patagonia incorporated into the Caron et al. (2018) ensemble is from Ivins et al. 2011.
750 Therefore, the prescribed GIA response across our domain does not perfectly match our simulated
751 ice history. Additionally, the global mantle from Caron et al. (2018) does not exhibit regional low
752 viscosity that is attributable to Patagonia and therefore, current rates of deformation are likely
753 underestimated by the model. By not simulating the 2-way coupled ice and solid-earth
754 interactions, we could be missing some feedbacks between our simulated ice history and the solid
755 earth that may modulate the deglaciation across this region. Despite this limitation however, our
756 prescribed GIA from Caron et al. (2018) is reasonable when compared with reconstructed deglacial
757 GIA in Patagonia (Troch et al., 2022; see Figure S2), giving confidence that our simulation is
758 capturing the regional influence of GIA on the simulated ice history.

760 Across most of our domain, ~~moraines formed of glacio-tectonized outwash (Bentley, 1996)~~
761 ~~provide~~ evidence for an advance of piedmont glaciers across glacial outwash during the LGM,
762 which formed the physical boundary for some of the existing terminal moraines around the lakes
763 within the CLD (Bentley, 1996; Bentley, 1997). The formation of ice-contact proglacial lakes
764 likely occurred as a function of deglacial warming ~~as~~ ice retreated ~~into overdeepenings in the~~
765 ~~bedrock topography and filled with meltwater~~ (Bentley, 1996). Where there were proglacial lakes
766 along the westward ice front in the CLD, evidence suggests that ice was grounded during the LGM
767 (Lago Puyehue; Heirman et al., 2011). ~~During deglaciation, proglacial lakes formed along the ice~~
768 ~~sheet margin (Bentley 1996,1997; Davies et al., 2020), with evidence suggesting that local~~
769 ~~topography and calving may have influenced the spatially varying retreat rates along these margins~~
770 ~~(Bentley, 1997).~~ Recent glacier modelling (Sutherland et al., 2020) suggests that inclusion of ice-
771 lake interactions may have large impacts on the magnitude and rate of simulated ice front retreat,
772 as ice-lake interactions promote greater ice velocities, ice flux to the grounding line, and surface
773 lowering. ~~However, it is not well constrained how the proglacial lakes in the CLD may have~~
774 ~~influenced local deglaciation (Heirman et al., 2011).~~ While more geomorphic data is needed,
775 ~~recent work south of our study region (46.5°S) reconstructed early deglacial ice retreat using a~~
776 ~~glaciolacustrine varve record from Lago General Carrera-Buenos Aires (Bendle et al., 2019).~~ The
777 ~~authors find that following initial retreat due to deglacial warming, the ice margin retreated into a~~

Deleted: there is

Deleted: and

Formatted: Font: 12 pt

Deleted: During deglaciation, iceberg calving into the proglacial lakes may have occurred (Bentley 1996,1997; Davies et al., 2020), with evidence suggesting that local topography and calving may have controlled the spatially irregular timing of abandonment from the terminal moraines surrounding the proglacial lakes (Bentley, 1997).

Formatted: Font: 12 pt

Formatted: Font: 12 pt

Formatted: Font: 12 pt

Formatted: Font: 12 pt

788 ~~deepening proglacial lake which accelerated ice retreat in this region due to persistent calving,~~
789 ~~therefore supporting the role proglacial lakes likely played across the margins of the retreating PIS~~
790 ~~during the last deglaciation.~~ Because the inclusion of ice-lake interactions is relatively novel for
791 numerical ice flow modeling (Sutherland et al., 2020; Quiquet et al., 2021; Hinck et al., 2022), we
792 choose to not simulate the evolution and influence of proglacial lakes on the deglaciation across
793 this model domain. Given this limitation, our simulated magnitude and rate of ice retreat at the
794 onset of deglaciation may be underestimated, especially when looking at local deglaciation along
795 these proglacial lakes. Although we do not think that these processes would greatly influence our
796 conclusions regarding the role of climate on the evolution of the PIS is the CLD and the simulated
797 ice retreat history, future work is required to assess the influence of proglacial lakes in this region.

799 5 Conclusions

801 In this study, we use a numerical ice sheet model to simulate the LGM and deglacial ice history
802 across the northernmost extent of the PIS, the CLD. The ice sheet model used inputs of
803 temperature and precipitation from the TraCE-21ka climate model simulation covering the last
804 22,000 years in order to simulate the deglaciation of the PIS across the CLD into the early
805 Holocene.

806
807 Our numerical simulation suggests that large scale ice retreat occurs after 19 ka coincident with
808 rapid deglacial warming, with the northern portion of the CLD becoming ice free by 17 ka. The
809 simulated ice retreat agrees well with the most comprehensive geologic assessment of past PIS
810 history available (PATICE; Davies et al., 2020) for the LGM ice extent and early deglacial but
811 diverge when considering the ice geometry at and after 15 ka. In our simulations, the PIS persists
812 until 15 ka across the remainder of the CLD, followed by ice retreat to higher elevations as
813 mountain glaciers and small ice caps persist into the early Holocene (e.g., Cerro Tronador). The
814 geologic reconstruction from PATICE instead estimates a small ice cap persisting across the
815 southern portion of high terrain in the CLD until about 10 ka. However, of the limited geologic
816 constraints particularly after 15 ka, high uncertainty in the timing and extent of deglacial ice history
817 remains in the geologic reconstruction. Therefore, our results provide an additional reconstruction
818 of the deglaciation of the PIS across the CLD that differs from PATICE after 15 ka, emphasizing
819 a need for future work that aims to improve geologic reconstructions of past ice margin migration
820 particularly during the later deglaciation across this region.

821
822 While deglacial warming was a primary driver of the demise of the PIS across the last deglaciation,
823 we find that precipitation modulates the pacing and magnitude of deglacial ice retreat across the
824 CLD. Paleoclimate proxies within the CLD has shown that the strength and position of the SWW
825 varied during the LGM and last deglaciation, altering hydrologic patterns and influencing the
826 deglacial mass balance. We find that the simulated changes in the strength and position of the
827 SWW in TraCE-21ka are similar to those inferred from paleoclimate proxies of precipitation,
828 consistent with a wetter than preindustrial climate being simulated and reconstructed over the CLD
829 and in particular the region north of 40°S. Through a series of sensitivity tests, we alter the
830 magnitude of the precipitation anomaly modestly (up to 10%) during our transient deglacial
831 simulations and find that the pacing of ice retreat can speed up or slow down by a few hundred
832 years and up to 2000 years depending on the imposed increase or decrease in the precipitation
833 anomaly. While paleoclimate proxies of precipitation suggest that the CLD may have experienced

Formatted: Font: 12 pt

Formatted: Font: 12 pt

Deleted: . However, across our region, Heirman et al. (2011) indicate that it is not well constrained how the proglacial lakes in the CLD may have influenced local deglaciation, as more geomorphic data is needed. Therefore,

Deleted: b

Formatted: Font: Not Bold, Pattern: Clear (White)

839 twice as much precipitation during the LGM and early deglacial relative to present day (Moreno
840 et al.,1999;2015), TraCE-21ka simulates smaller increases in LGM and early deglacial
841 precipitation (~10-15% greater than preindustrial). Therefore, while our modelling suggests that
842 modest changes in precipitation can modulate the pace of deglacial ice retreat across the CLD,
843 from our analysis we can deduce that larger anomalies in precipitation as found in the paleoclimate
844 proxies may have an even larger impact on modulating deglacial ice retreat. Because paleoclimate
845 proxies of past precipitation are often lacking, and climate models can simulate a range of possible
846 LGM and deglacial hydrologic states, these results suggest that improved knowledge of the past
847 precipitation is critical towards better understanding the drivers of PIS growth and demise,
848 especially as small variations in precipitation can modulate ice sheet history on scales consistent
849 with geologic proxies.

850
851 **Code/Data Availability**

852 The simulations performed for this paper made use of the open-source Ice-Sheet and Sea-level
853 System Model (ISSM) and are publicly available at <https://issm.jpl.nasa.gov/> (Larour et al., 2012).

854
855 **Author Contribution**

856 JC and SM secured funding for this research. JC, MR, and SM all contributed to the project design.
857 JC performed the model setup and simulations. JC performed the analyses on model output, with
858 help from MR who performed analysis on PATICE reconstructions. JC wrote the manuscript with
859 input from MR and SM.

860
861 **Competing interests**

862 The contact author has declared that none of the authors has any competing interests.

863
864 **Acknowledgements**

865 This work was supported by a grant from the National Science Foundation, Frontier Research in
866 Earth Sciences # 2121561. We would like to thank Lambert Caron from the Jet Propulsion
867 Laboratory for his input regarding Glacial Isostatic Adjustment across our study region.

868
869 **References**

870 Adhikari, S., Ivins, E. R., and Larour, E., 2016, ISSM-SESAW v1.0: mesh-based computation of
871 gravitationally consistent sea level and geodetic signatures caused by cryosphere and
872 climate driven mass change, *Geoscientific Model Development*, 9, 9769-9816, doi:
873 10.5194/gmd-9-1087-2016.

874 Åkesson, H., Morlighem, M., Nisancioglu, K. H., Svendsen, J. J., and Mangerud, J.:
875 Atmosphere-driven ice sheet mass loss paced by topography: Insights from modelling the
876 south-western Scandinavian Ice Sheet. 2018. *Quaternary Sci. Rev.*, 195, 32–
877 47, <https://doi.org/10.1016/j.quascirev.2018.07.004>.

878 Andersen, B., Denton, G. H., & Lowell, T. V. (1999). Glacial geomorphologic maps of
879 Llanquihue drift in the area of the southern Lake District, Chile. *Geografiska Annaler:*
880 *Series A, Physical Geography*, 81(2), 155-166.

881 [Bendle, J.M., Palmer, A.P., Thorndycraft, V.R., Matthews, I.P. 2019. Phased Patagonian Ice
882 Sheet response to Southern Hemisphere atmospheric and oceanic warming between 18
883 and 17 ka. *Sci. Rep.* 9, 4133. <https://doi.org/10.1038/s41598-019-39750-w>](#)

884 Bentley, M.J., 1996. The role of lakes in moraine formation, Chilean Lake District. *Earth*

Formatted: Font: 12 pt

Formatted: Font: 12 pt

Formatted: Indent: First line: 0", Adjust space between Latin and Asian text, Adjust space between Asian text and numbers

Formatted: Font color: Auto, Pattern: Clear

885 Surf. Process. Landf. 21, 493–507. [https://doi.org/10.1002/\(SICI\)1096-](https://doi.org/10.1002/(SICI)1096-)
886 9837(199606)21:6<493::AID-ESP612>3.0.CO;2-D

887 Bentley, M.J., 1997. Relative and radiocarbon chronology of two former glaciers in the
888 Chilean Lake District. *J. Quat. Sci.* 12, 25–33. [https://doi.org/10.1002/\(SICI\)1099-](https://doi.org/10.1002/(SICI)1099-)
889 1417(199701/02)12:1<25::AID-JQS289>3.0.CO;2-A

890 Berman, L., Silvestri, G., Tonello, M.S., On differences between Last Glacial Maximum and
891 Mid-Holocene climates in southern South America simulated by PMIP3 models. 2018.
892 *Quat. Sci. Rev.* 185, 113-121. <https://doi.org/10.1016/j.quascirev.2018.02.003>.

893 Blatter, H.: Velocity and stress-fields in grounded glaciers: A simple algorithm for including
894 deviatoric stress gradients. 1995. *J. Glaciol.*, 41, 333-344,
895 <https://doi.org/10.3189/S002214300001621X>

896 Boex, J., Fogwill, C., Harrison, S. et al. Rapid thinning of the late Pleistocene Patagonian Ice
897 Sheet followed migration of the Southern Westerlies. 2013. *Sci Rep* 3, 2118.
898 <https://doi.org/10.1038/srep02118>

899 Boisier, J. P., Alvarez-Garretón, C., Cepeda, J., Osses, A., Vásquez, N., and Rondanelli, R.:
900 CR2MET: A high-resolution precipitation and temperature dataset for hydroclimatic
901 research in Chile. 2018. EGUGA, p. 19739.

902 Braun, M.H., Malz, P., Sommer, C., Far.as-Barahona, D., Sauter, T., Casassa, G., Soruco,
903 A., Skvarca, P., Seehaus, T.C., 2019. Constraining glacier elevation and mass changes
904 in South America. *Nat. Clim. Chang.* 9, 130–136. <https://doi.org/10.1038/s41558-018->
905 0375-7

906 Brierley, C. M., Zhao, A., Harrison, S. P., Braconnot, P., Williams, C. J. R., Thornalley, D. J. R.,
907 Shi, X., Peterschmitt, J.-Y., Ohgaito, R., Kaufman, D. S., Kageyama, M., Hargreaves, J.
908 C., Erb, M. P., Emile-Geay, J., D'Agostino, R., Chandan, D., Carré, M., Bartlein, P. J.,
909 Zheng, W., Zhang, Z., Zhang, Q., Yang, H., Volodin, E. M., Tomas, R. A., Routson, C.,
910 Peltier, W. R., Otto-Bliesner, B., Morozova, P. A., McKay, N. P., Lohmann, G., Legrande,
911 A. N., Guo, C., Cao, J., Brady, E., Annan, J. D., and Abe-Ouchi, A.: Large-scale features
912 and evaluation of the PMIP4-CMIP6 *midHolocene* simulations, *Clim. Past*, 16, 1847–
913 1872, <https://doi.org/10.5194/cp-16-1847-2020>, 2020.

914 Briner, J. P., Cuzzzone, J. K., Badgeley, J. A., Young, N. E., Steig, E. J., Morlighem, M.,
915 Schlegel, N.-J., Hakim, G., Schaefer, J. Johnson, J. V., Lesnek, A. L., Thomas, E. K.,
916 Allan, E., Bennike, O., Cluett, A. A., Csatho, B., de Vernal, A., Downs, J., Larour, E.,
917 and Nowicki, S.: Rate of mass loss from the Greenland Ice Sheet will exceed Holocene
918 values this century. 2020. *Nature*, 6, 70–74, <https://doi.org/10.1038/s41586-020-2742-6>.

919 Bondzio, J. H., Seroussi, H., Morlighem, M., Kleiner, T., Rückamp, M., Humbert, A., and
920 Larour, E. Y.: Modelling calving front dynamics using a level-set method: application to
921 Jakobshavn Isbræ, West Greenland. 2016. *The Cryosphere*, 10, 497–
922 510, <https://doi.org/10.5194/tc-10-497-2016>

923 Budd, W.F., P. L. Keage, N. A. Blundy. Empirical studies of ice sliding. 1979. *J. Glaciol.*,
924 23:157-170.

925 Caron, L., Ivins, E. R., Larour, E., Adhikari, S., Nilsson, J., and Blewitt, G.: GIA model statistics
926 for GRACE hydrology, cryosphere and ocean science. 2018. *Geophys. Res. Lett.*, 45,
927 2203–2212, <https://doi.org/10.1002/2017GL076644>

928 Choi, Y., Morlighem, M., Rignot, E., and Wood, M.: Ice dynamics will remain a primary driver
929 of Greenland ice sheet mass loss over the next century. 2021. *Commun. Earth Environ.*,
930 2, 26, <https://doi.org/10.1038/s43247-021-00092-z>

931 Clark, P.U., He, F., Gollledge, N.R., Mitrovica, J.X., Dutton, A., Hoffman, J.S., and Dendy, S.,
932 2020, Oceanic forcing of penultimate deglacial and last interglacial sea-level rise: Nature,
933 v. 577, p. 660–664, doi:10.1038/s41586-020-1931-7.

934 Cuffey, K. M. and Paterson, W. S. B.: The physics of glaciers, 4th edn. 2010. Butterworth-
935 Heinemann, Oxford, ISBN 9780123694614

936 Cuzzone, J. K., Schlegel, N.-J., Morlighem, M., Larour, E., Briner, J. P., Seroussi, H., and Caron,
937 L.: The impact of model resolution on the simulated Holocene retreat of the southwestern
938 Greenland ice sheet using the Ice Sheet System Model (ISSM). 2019. The Cryosphere,
939 13, 879–893, <https://doi.org/10.5194/tc-13-879-2019>.

940 Cuzzone, J. K., Young, N. E., Morlighem, M., Briner, J. P., and Schlegel, N.-J.: Simulating the
941 Holocene deglaciation across a marine-terminating portion of southwestern Greenland in
942 response to marine and atmospheric forcings. 2022. The Cryosphere, 16, 2355–2372,
943 <https://doi.org/10.5194/tc-16-2355-2022>.

944 Davies, B.J., Darvill, C.M., Lovell, H., Bendle, J.M., Dowdeswell, J.A., Fabel, D.,
945 Gheorghiu, D.M., 2020. The evolution of the Patagonian ice sheet from 35 ka to
946 the present day (PATICE). Earth Sci. Rev. 204, 103152. [https://doi.org/10.1016/](https://doi.org/10.1016/j.earscirev.2020.103152)
947 [j.earscirev.2020.103152](https://doi.org/10.1016/j.earscirev.2020.103152).

948 Darvill., C.M., Stokes, C.R., Bentley, M.J., Evans, D.J.A., Lovell, H. 1996. Dynamics of former
949 ice lobes of the southernmost Patagonian Ice Sheet based on glacial landsystems
950 approach. Journal of Quaternary Science. 32, 6, 857-876.
951 <https://doi.org/10.1002/jqs.2890>

952 Darvill, C.M., Stokes, C.R., Bentley, M.J., Evans, D.J.A., Lovell, H., Dynamics of former ice
953 lobes of the southernmost Patagonian Ice Sheet based on glacial landsystems approach.
954 2017. J. Quaternary Sci., 32:857-876. <https://doi.org/10.1002/jqs.2890>

955 Denton, G.H., Lowell, T.V., Heusser, C.J., Schlüchter, C., Andersen, B.G., Heusser, L.E.,
956 Moreno, P.I., Marchant, D.R., 1999. Geomorphology, Stratigraphy, and Radiocarbon
957 Chronology of Llanquihue Drift in the Area of the Southern Lake District, Seno
958 Reloncav., and Isla Grande de Chilo., Chile. Geogr. Ann. Ser. A Phys. Geogr. 81,
959 167–229. <https://doi.org/10.1111/1468-0459.00057>

960 Denton, G.H., Heusser, J., Lowell, T.V., Moreno, P.I., Andersen, B.G., Heusser, L.E., Schlüchter,
961 C., Marchant, D.R. 1999. Interhemispheric Linkage of Paleoclimate During the Last
962 Glaciation. Geografiska Annaler. 81, 2, 107-153. [https://doi.org/10.1111/1468-](https://doi.org/10.1111/1468-0459.00055)
963 [0459.00055](https://doi.org/10.1111/1468-0459.00055)

964 Dias dos Santos, T., Morlighem, M., and Brinkerhoff, D.: A new vertically integrated MONo-
965 Layer Higher-Order (MOLHO) ice flow model. 2022. The Cryosphere, 16, 179–195,
966 <https://doi.org/10.5194/tc-16-179-2022>.

967 Díaz, C., Moreno, P. I., Villacís, L. A., Sepúlveda-Zúñiga, E. A., & Maidana, N. I. (2023).
968 Freshwater diatom evidence for Southern Westerly Wind evolution since~ 18 ka in
969 northwestern Patagonia. Quaternary Science Reviews, 316, 108231.

970 Fernandez, A., Mark, B.G. 2016. Modeling modern glacier response to climate changes along the
971 Andes Cordillera: A multiscale review, J. Adv. Model. Earth Syst., 8, 467–495,
972 doi:10.1002/2015MS000482.

973 [García, J. L., Maldonado, A., De Porras, M. E., Delaunay, A. N., Reyes, O., Ebensperger, C. A.,](https://doi.org/10.1017/qua.2018.93)
974 [Binnie, Lüthgens, C., S.A., Méndez, C. 2019. Early deglaciation and paleolake history of](https://doi.org/10.1017/qua.2018.93)
975 [Río Cisnes glacier, Patagonian ice sheet \(44 S\). Quaternary Research, 91\(1\), 194-217.](https://doi.org/10.1017/qua.2018.93)
976 <https://doi.org/10.1017/qua.2018.93>.

Formatted: Font: (Default) Times New Roman, 12 pt

Formatted: Indent: Left: 0", Hanging: 0.5"

Formatted: Default Paragraph Font, Font: (Default) Times New Roman, 12 pt, Font color: Auto

Formatted: Font: (Default) Times New Roman, 12 pt

Formatted: Font: (Default) Times New Roman, 12 pt

977
978 Garreaud, R., Lopez, P., Minvielle, M., & Rojas, M. (2013). Large-scale control on the
979 Patagonian climate. *Journal of Climate*, 26(1), 215-230.
980 GEBCO Bathymetric Compilation Group 2021. 2021. The GEBCO_2021 Grid - a continuous
981 terrain model of the global oceans and land. NERC EDS British Oceanographic Data
982 Centre NOC. doi:10.5285/c6612cbe-50b3-0cff-e053-6c86abc09f8f
983 Glasser, N. F., Jansson, K. N., Harrison, S., & Kleman, J. (2008). The glacial geomorphology
984 and Pleistocene history of South America between 38 S and 56 S. *Quaternary Science*
985 *Reviews*, 27(3-4), 365-390.
986 Glen, J. W. The creep of polycrystalline ice. 1955. *P. Roy. Soc. Lond. A*, 228, 519–
987 538, <https://doi.org/10.1098/rspa.1955.0066>.
988 Gollledge, N. R., Thomas, Z. A., Levy, R. H., Gasson, E. G. W., Naish, T. R., McKay, R. M.,
989 Kowalewski, D. E., and Fogwill, C. J.: Antarctic climate and ice-sheet configuration
990 during the early Pliocene interglacial at 4.23 Ma, *Clim. Past*, 13, 959–975,
991 <https://doi.org/10.5194/cp-13-959-2017>, 2017.
992 [Hartmann, D. and Lo, F. Wave-Driven Zonal Flow Vacillation in the Southern Hemisphere.](#)
993 [1998. *Journal of the Atmospheric Sciences*. 55, 8, 1303-1315.](#)
994 [https://doi.org/10.1175/1520-0469\(1998\)055<1303:WDZFFVI>2.0.CO;2](https://doi.org/10.1175/1520-0469(1998)055<1303:WDZFFVI>2.0.CO;2)
995 Hajima, T., Watanabe, M., Yamamoto, A., Tatebe, H., Noguchi, M. A., Abe, M., Ohgaito, R.,
996 Ito, A., Yamazaki, D., Okajima, H., Ito, A., Takata, K., Ogochi, K., Watanabe, S., and
997 Kawamiya, M.: Development of the MIROC-ES2L Earth system model and the
998 evaluation of biogeochemical processes and feedbacks, *Geosci. Model Dev.*, 13, 2197–
999 2244, <https://doi.org/10.5194/gmd-13-2197-2020>
1000 He, F., Shakun, J. D., Clark, P. U., Carlson, A. E., Liu, Z., Otto-Bliesner, B. L., Kutzbach, J. E.
1001 2013. Northern Hemisphere forcing of Southern Hemisphere climate during the last
1002 deglaciation, *Nature*, 494, 81–85. doi: 10.1038/nature11822.
1003 He, F., Clark, P.U. 2022. Freshwater forcing of the Atlantic Meridional Overturning Circulation
1004 revisited. *Nature Climate Change*. 12. 449-454. [https://doi.org/10.1038/s41558-022-](https://doi.org/10.1038/s41558-022-01328-2)
1005 [01328-2](https://doi.org/10.1038/s41558-022-01328-2).
1006 Heirman, K., De Batist, M., Charlet, F., Moernaut, J., Chapron, E., Brümmner, R., Pino, M.,
1007 Urrutia, R., 2011. Detailed seismic stratigraphy of Lago Puyehue: implications for the
1008 mode and timing of glacier retreat in the Chilean Lake District. *J. Quat. Sci.* 26,
1009 665–674. <https://doi.org/10.1002/jqs.1491>
1010 Hinck, S., Gowan, E. J., Zhang, X., and Lohmann, G.: PISM-LakeCC: Implementing an adaptive
1011 proglacial lake boundary in an ice sheet model. 2022. *The Cryosphere*, 16, 941–965,
1012 <https://doi.org/10.5194/tc-16-941-2022>.
1013 Hubbard, A., Hein, A.S., Kaplan, M.R., Hulton, N.R.J., Glasser, N., 2005. A modelling
1014 reconstruction of the last glacial maximum ice sheet and its deglaciation in the
1015 vicinity of the northern patagonian icefield, south America. *Geogr. Ann. Phys.Geogr.* 87
1016 (2), 375-391. <https://doi.org/10.1111/j.0435-3676.2005.00264.x>
1017 Hulton, N.R.J., Purves, R., McCulloch, R., Sugden, D.E., Bentley, M.J., 2002. The last
1018 glacial maximum and deglaciation in southern south America. *Quat. Sci. Rev.* 21
1019 (1), 233-241. [https://doi.org/10.1016/S0277-3791\(01\)00103-2](https://doi.org/10.1016/S0277-3791(01)00103-2).
1020 Hulton, N., Sugden, D., Payne, A., Clapperton, C., 1994. Glacier modeling and the
1021 climate of Patagonia during the last glacial maximum. *Quat. Res.* 42 (1), 1-19.
1022 doi:10.1006/qres.1994.1049

Formatted: Font: Times New Roman, No underline

1023 Jiang, N., Yan, Q. Evolution of the meridional shift of the subtropical and subpolar westerly jet
 1024 over the Southern Hemisphere during the past 21,000 years. 2020. *Quat Sci. Rev.* 246,
 1025 <https://doi.org/10.1016/j.quascirev.2020.106544>.

1026 ~~Kaplan, M. R., Ackerly Jr, R. P., Singer, B. S., Douglass, D. C., & Kurz, M. D. 2004. Cosmogenic
 1027 nuclide chronology of millennial-scale glacial advances during O-isotope stage 2 in
 1028 Patagonia. *Geological Society of America Bulletin*, 116(3-4), 308-321. doi:
 1029 10.1130/B25178.1~~

1030 ~~Kaplan, M. R., Fogwill, C. J., Sugden, D. E., Hulton, N. R. J., Kubik, P. W., & Freeman, S. P. H.
 1031 T. 2008. Southern Patagonian glacial chronology for the Last Glacial period and
 1032 implications for Southern Ocean climate. *Quaternary Science Reviews*, 27(3-4), 284-294.
 1033 <https://doi.org/10.1016/j.quascirev.2007.09.013>~~

1034 Kilian, R., Lamy, F., 2012. A review of Glacial and Holocene paleoclimate records
 1035 from southernmost Patagonia (49e55 S). *Quat. Sci. Rev.* 53,
 1036 doi.10.1016/j.quascirev.2012.07.017

1037 Kageyama, M., Harrison, S. P., Kapsch, M.-L., Lofverstrom, M., Lora, J. M., Mikolajewicz, U.,
 1038 Sherriff-Tadano, S., Vadsaria, T., Abe-Ouchi, A., Bouttes, N., Chandan, D., Gregoire, L.
 1039 J., Ivanovic, R. F., Izumi, K., LeGrande, A. N., Lhardy, F., Lohmann, G., Morozova, P.
 1040 A., Ohgaito, R., Paul, A., Peltier, W. R., Poulsen, C. J., Quiquet, A., Roche, D. M., Shi,
 1041 X., Tierney, J. E., Valdes, P. J., Volodin, E., and Zhu, J. 2021. The PMIP4 Last Glacial
 1042 Maximum experiments: preliminary results and comparison with the PMIP3 simulations,
 1043 *Clim. Past*, 17, 1065–1089, <https://doi.org/10.5194/cp-17-1065-2021>.

1044 Kilian, R., Lamy, F. A review of Glacial and Holocene paleoclimate records from southernmost
 1045 Patagonia (49-55°S). 2012. 53, 15, 1-23.
 1046 <https://doi.org/10.1016/j.quascirev.2012.07.017>

1047 Kohfeld, K.E., Graham, R.M., Boer, A. M. de, Sime, L.C., Wolff, E.W., Qu er e, C.L.,
 1048 Bopp, L., 2013. Southern Hemisphere westerly wind changes during the Last
 1049 Glacial Maximum: paleo-data synthesis. *Quat. Sci. Rev.* 68, 76-95. ,
 1050 10.1016/j.quascirev.2013.01.017

1051 Lamy, F., Kilian, R., Arz, H.W., Francois, J.-P., Kaiser, J., Prange, M., Steinke, T., 2010.
 1052 Holocene changes in the position and intensity of the southern westerly wind belt. *Nat.*
 1053 *Geosci.* 3, 695–699. <https://doi.org/10.1038/ngeo959>

1054 Lamy, F., Arz, H. W., Kilian, R., Lange, C. B., Lembke-Jene, L., Wengler, M., ... & Tiedemann,
 1055 R. (2015). Glacial reduction and millennial-scale variations in Drake Passage
 1056 throughflow. *Proceedings of the National Academy of Sciences*, 112(44), 13496-13501
 1057 <https://doi.org/10.1073/pnas.1509203112>

1058 Larour, E., Seroussi, H., Morlighem, M., and Rignot, E.: Continental scale, high order, high
 1059 spatial resolution, ice sheet modeling using the Ice Sheet System Model (ISSM). 2012. *J.*
 1060 *Geophys. Res.-Earth*, 117, F01022, <https://doi.org/10.1029/2011JF002140>

1061 Le Morzadec, K., Tarasov, L., Morlighem, M., and Seroussi, H.: A new sub-grid surface mass
 1062 balance and flux model for continental-scale ice sheet modelling: testing and last glacial
 1063 cycle. 2015. *Geosci. Model Dev.*, 8, 3199–3213, [https://doi.org/10.5194/gmd-8-3199-](https://doi.org/10.5194/gmd-8-3199-2015)
 1064 [2015](https://doi.org/10.5194/gmd-8-3199-2015),

1065 ~~Leger, T. P., Hein, A. S., Bingham, R. G., Rodés, Á., Fabel, D., & Smedley, R. K. 2021a.
 1066 *Geomorphology and 10Be chronology of the Last Glacial Maximum and deglaciation in*
 1067 *northeastern Patagonia, 43° S-71° W. Quaternary Science Reviews*, 272, 107194.
 1068 DOI:10.1016/j.quascirev.2021.107194~~

Formatted: Default Paragraph Font, Font color: Text 1

Formatted: Font: (Default) Times New Roman, 12 pt

Formatted: Font: (Default) Times New Roman, 12 pt

Formatted: Indent: Left: 0", Hanging: 0.5"

Formatted: Font: (Default) Times New Roman, 12 pt

Deleted: ¶

Formatted: Default Paragraph Font, Font color: Text 1

Deleted:

Formatted: Font: (Default) Times New Roman, 12 pt

Formatted: Indent: Left: 0", Hanging: 0.5"

Formatted: Font: Times New Roman, 12 pt

Formatted: Font: Times New Roman, 12 pt

Formatted: Font: (Default) Times New Roman, 12 pt

1071 Leger TPM, Hein AS, Goldberg D, Schimmelpfennig I, Van Wyk de Vries MS, Bingham RG and
1072 ASTER Team. 2021b. Northeastern Patagonian Glacier Advances (43°S) Reflect
1073 Northward Migration of the Southern Westerlies Towards the End of the Last Glaciation.
1074 Front. Earth Sci. 9:751987. doi: 10.3389/feart.2021.751987
1075 Liu, Z., Otto-Bliesner, B., He, F., Brady, E., Tomas, R., Clark, P., Carlson, A., Lynch-Stieglitz,
1076 J., Curry, W., Brook, E., Erickson, D., Jacob, R., Kutzbach, J., and Cheng, J. 2009.
1077 Transient simulation of last deglaciation with a new mechanism for Bølling-Allerød
1078 warming, Science, 325, 310–314. <https://doi.org/10.1126/science.1171041>
1079 Lowry, D. P., Golledge, N. R., Menviel, L., and Bertler, N. A. N.: Deglacial evolution of
1080 regional Antarctic climate and Southern Ocean conditions in transient climate
1081 simulations. 2019. Clim. Past, 15, 189–215, <https://doi.org/10.5194/cp-15-189-2019>.
1082 Lowell, T., Heusser, C., Andersen, B., Moreno, P., Hauser, A., Heusser, L., Schlüchter,
1083 C., Marchant, D., Denton, G., 1995. Interhemispheric correlation of late Pleistocene glacial
1084 events. Science 269, 1541–1549. Doi: 10.1126/science.269.5230.1541

1085 Lowry, D. P., Golledge, N. R., Menviel, L., and Bertler, N. A. N.: Deglacial evolution of
1086 regional Antarctic climate and Southern Ocean conditions in transient climate
1087 simulations. 2019. Clim. Past, 15, 189–215, <https://doi.org/10.5194/cp-15-189-2019>
1088 Marcott, S.A., Shakun, J.D., Clark, P.U., Mix, A.C. 2013. A Reconstruction of Regional and
1089 Global Temperature for the Past 11,300 Years. 339, 6124, 1198-1201. DOI:
1090 10.1126/science.1228026

1091 Martin J, Davies BJ, Jones R and Thorndyraft V (2022), Modelled sensitivity of Monte San
1092 Lorenzo ice cap, Patagonian Andes, to past and present climate. Front. Earth Sci.
1093 10:831631. doi: 10.3389/feart.2022.831631

1094 Mauritsen, T., Bader, J., Becker, T., Behrens, J., Bittner, M., Brokopf, R., Brovkin, V., Claussen,
1095 M., Crueger, T., Esch, M., Fast, I., Fiedler, S., Fläschner, D., Gayler, V., Giorgetta, M.,
1096 Goll, D. S., Haak, H., Hagemann, S., Hedemann, C., Hohenegger, C., Ilyina, T., Jahns, T.,
1097 Jimenez-de-la-Cuesta, D., Jungclaus, J., Kleinen, T., Kloster, S., Kracher, D., Kinne, S.,
1098 Kleberg, D., Lasslop, G., Kornbluh, L., Marotzke, J., Matei, D., Meraner, K.,
1099 Mikolajewicz, U., Modali, K., Möbis, B., Müller, W. A., Nabel, J. E. M. S., Nam, C. C.
1100 W., Notz, D., Nyawira, S.-S., Paulsen, H. Peters, K., Pincus, R., Pohlmann, H. Pongratz,
1101 J., Popp, M., Raddatz, T. J., Rast, S., Redler, R., Reick, C. H., Rohrschneider, T.,
1102 Schemann, V., Schmidt, H., Schnur, R., Schulzweida, U., Six, K. D., Stein, L., Stemmler,
1103 I., Stevens, B., von Storch, J.-S., Tian, F., Voigt, A., Vrese, P., Wieners, K.-H.,
1104 Wilkenskeld, S., Winkler, A., and Roeckner, E.: Developments in the MPI-M Earth
1105 System Model version 1.2 (MPI-ESM1.2) and its response to increasing CO₂, J. Adv.
1106 Model. Earth Syst. 2019. 11, 998–1038, <https://doi.org/10.1029/2018MS001400>

1107 McCulloch, R. D., Bentley, M. J., Purves, R. S., Hulton, N. R., Sugden, D. E., & Clapperton, C.
1108 M. (2000). Climatic inferences from glacial and palaeoecological evidence at the last
1109 glacial termination, southern South America. *Journal of Quaternary Science: Published*
1110 *for the Quaternary Research Association*, 15(4), 409-417.
1111 <https://doi.org/10.1002/jqs.608>

1112 McCulloch, R. D., Fogwill, C. J., Sugden, D. E., Bentley, M. J., & Kubik, P. W. (2005).
1113 Chronology of the last glaciation in central Strait of Magellan and Bahía Inútil,
1114 southernmost South America. *Geografiska Annaler: Series A, Physical*
1115 *Geography*, 87(2), 289-312. <https://doi.org/10.1111/j.0435-3676.2005.00260.x>

Deleted: ¶

Deleted: (

Deleted:)

Formatted: Font: (Default) Times New Roman, 12 pt

Formatted: Indent: Left: 0", Hanging: 0.5"

Formatted: Font: (Default) Times New Roman, 12 pt, Font color: Text 1

Formatted: Font color: Text 1

Formatted: Font: (Default) Times New Roman, 12 pt, Font color: Text 1

Formatted: Font color: Text 1

Formatted: Font: (Default) Times New Roman, 12 pt, Not Bold

Field Code Changed

Formatted: Font: (Default) Times New Roman, 12 pt

Formatted: Normal, Indent: Left: 0", Hanging: 0.5", No bullets or numbering, Pattern: Clear (White)

Formatted: Default Paragraph Font, Font: (Default) Times New Roman, 12 pt, Font color: Dark Gray

Formatted: Font: (Default) Times New Roman, 12 pt, Font color: Text 1

1119 Meier, W.J-H., Griesbinger, J., Hochreuther, P., Braun, M.H. 2018. An updated multi-temporal
 1120 glacier inventory for the Patagonian Andes with changes between the Little Ice Age and
 1121 2016. *Frontiers in Earth Science*, 6, 62. <https://doi.org/10.3389/feart.2018.00062>
 1122 Menviel, L., A. Timmermann, A. Mouchet, and O. Timm, 2008: Climate and marine carbon
 1123 cycle response to changes in the strength of the Southern Hemispheric
 1124 westerlies. *Paleoceanography*, **23**, PA4201, doi:10.1029/2008PA001604.
 1125 Mercer, J.H., 1972. Chilean glacial chronology 20,000 to 11,000 carbon-14 years ago:some
 1126 global comparisons. *Science* 176, 1118–1120. DOI: 10.1126/science.176.4039.1118
 1127 Moreno, P. I., Lowell, T. V., Jacobson Jr, G. L., & Denton, G. H. (1999). Abrupt vegetation and
 1128 climate changes during the last glacial maximum and last termination in the Chilean lake
 1129 district: a case study from Canal de la Puntilla (41 s). *Geografiska Annaler: Series A*,
 1130 *Physical Geography*, 81(2), 285-311.
 1131 Moreno, P.I., Denton, G.H., Moreno, H., Lowell, T.V., Putnam, A.E., Kaplan, M.R., 2015.
 1132 Radiocarbon chronology of the last glacial maximum and its termination in
 1133 northwestern Patagonia. *Quat. Sci. Rev.* 122, 233e249. 10.1016/j.quascirev.2015.05.027
 1134 Moreno, P.I., Videla, J., Valero-Garcés, B.L., Alloway, B.V., Heusser, L.E., 2018.
 1135 A continuous record of vegetation, fire-regime and climatic changes in northwestern
 1136 Patagonia spanning the last 25,000 years. *Quat. Sci. Rev.* 198,
 1137 10.1016/j.quascirev.2018.08.013
 1138 Morlighem, M., Bondzio, J., Seroussi, H., Rignot, E., Larour, E., Humbert, A., and Rebuffi, S.:
 1139 Modeling of Store Gletscher's calving dynamics, West Greenland, in response to ocean
 1140 thermal forcing. 2016. *Geophys. Res. Lett.*, 43, 2659–
 1141 2666, <https://doi.org/10.1002/2016GL067695>
 1142 Muir, R., Eaves, S., Vargo, L., Anderson, B., Mackintosh, A., Sagredo, E., Soteres, R. Late
 1143 glacial climate evolution in the Patagonian Andes (44-47°S) from alpine glacier modelling.
 1144 2023. *Quaternary Science Reviews*, 305, <https://doi.org/10.1016/j.quascirev.2023.108035>.
 1145 Ohgaito, R., Yamamoto, A., Hajima, T., Oishi, R., Abe, M., Tatebe, H., Abe-Ouchi, A., and
 1146 Kawamiya, M.: PMIP4 experiments using MIROC-ES2L Earth system model, *Geosci.*
 1147 *Model Dev.*, 14, 1195–1217, <https://doi.org/10.5194/gmd-14-1195-2021>
 1148 Pattyn, F.: A new three-dimensional higher-order thermomechanical ice sheet model:
 1149 Basic sensitivity, ice stream development, and ice flow across subglacial lakes. 2003. *J.*
 1150 *Geophys. Res.*, 108, 2382, <https://doi.org/10.1029/2002JB002329>
 1151 Pedro, J. B., Bostock, H. C., Bitz, C. M., He, F., Vandergoes, M. J., Steig, E. J., Chase, B.M.,
 1152 Krause, C.E., Rasmussen, S.O., Bradley, M.R., Cortese, G. 2016. The spatial extent and
 1153 dynamics of the Antarctic Cold Reversal. *Nature Geoscience*, 9(1), 51-55.
 1154 <https://doi.org/10.1038/ngeo2580>
 1155 Peixoto, J. P., and A. H. Oort (1992), *Physics of Climate*, American Institute of Physics,
 1156 520 pp.
 1157 Peltier, C., Kaplan, M. R., Birkel, S. D., Soteres, R. L., Sagredo, E. A., Aravena, J. C., ... &
 1158 Schaefer, J. M. (2021). The large MIS 4 and long MIS 2 glacier maxima on the southern
 1159 tip of South America. *Quaternary Science Reviews*, 262, 106858.
 1160 <https://doi.org/10.1016/j.quascirev.2021.106858> 0277-3791
 1161 Peltier, C., Kaplan, M. R., Sagredo, E. A., Moreno, P. I., Araos, J., Birkel, S. D., ... & Schaefer,
 1162 J. M. (2023). The last two glacial cycles in central Patagonia: A precise record from the
 1163 Ñirehuao glacier lobe. *Quaternary Science Reviews*, 304, 107873.
 1164 [DOI:10.1016/j.quascirev.2022.107873](https://doi.org/10.1016/j.quascirev.2022.107873)

Deleted: ¶

Formatted: Font: (Default) Times New Roman, 12 pt

Formatted: Font: (Default) Times New Roman, 12 pt

Formatted: Indent: Left: 0", Hanging: 0.5"

Formatted: Font: Times New Roman, 12 pt

Formatted: Default Paragraph Font, Font: Times New Roman, 12 pt

Formatted: Font: (Default) Times New Roman, 12 pt

1166
1167 Pfeffer, W.T., Arendt, A.A., Bliss, A., Bolch, T., Cogley, J.G., Gardner, A.S., Hagen, J.O., Hock,
1168 R., Kaser, G., Kienholz, C. and Miles, E.S. 2014. The Randolph Glacier Inventory: a
1169 globally complete inventory of glaciers. *Journal of Glaciology*, 60, 537-552.
1170 Doi:10.31.3189/2014JoG13J176
1171 Pollard, D. and DeConto, R. M.: Description of a hybrid ice sheet-shelf model, and application to
1172 Antarctica. 2012. *Geosci. Model Dev.*, 5, 1273–1295, <https://doi.org/10.5194/gmd-5-1273-2012>.
1173
1174 Porter, S. C. (1981). Pleistocene glaciation in the southern Lake District of Chile. *Quaternary*
1175 *Research*, 16(3), 263-292.
1176 Quiquet, A., Dumas, C., Paillard, D., Ramstein, G., Ritz, C., and Roche, D. M.: Deglacial Ice
1177 Sheet Instabilities Induced by Proglacial Lakes. 2021. *Geophys. Res. Lett.*, 48,
1178 e2020GL092141, <https://doi.org/10.1029/2020GL092141>
1179 Rojas, M., Moreno, P., Kageyama, M., Crucifix, M., Hewitt, C., Abe-Ouchi, A., Ohgaito, R.,
1180 Brady, E.C., Hop, P. 2009. The Southern Westerlies during the last glacial maximum in
1181 PMIP2 simulations. *Clim. Dyn.* 32, 525–548. <https://doi.org/10.1007/s00382-008-0421-7>.
1182
1183 Rojas, M., 2013. Sensitivity of southern Hemisphere circulation to LGM and 4 CO₂
1184 climates. *Geophys. Res. Lett.* 40, 965e970.
1185 Sepulchre, P., Caubel, A., Ladant, J.-B., Bopp, L., Boucher, O., Braconnot, P., Brockmann, P.,
1186 Cozic, A., Donnadieu, Y., Dufresne, J.-L., Estella-Perez, V., Ethé, C., Fluteau, F.,
1187 Foujols, M.-A., Gastineau, G., Ghattas, J., Hauglustaine, D., Hourdin, F., Kageyama, M.,
1188 Khodri, M., Marti, O., Meurdesoif, Y., Mignot, J., Sarr, A.-C., Servonnat, J.,
1189 Swingedouw, D., Szopa, S., and Tardif, D.: IPSL-CM5A2 – an Earth system model
1190 designed for multi-millennial climate simulations, *Geosci. Model Dev.*, 2020. 13, 3011–
1191 3053, <https://doi.org/10.5194/gmd-13-3011-2020>
1192 Seguinot, J., Rogozhina, I., Stroeven, A. P., Margold, M., and Kleman, J.: Numerical simulations
1193 of the Cordilleran ice sheet through the last glacial cycle, *The Cryosphere*, 10, 639–664,
1194 <https://doi.org/10.5194/tc-10-639-2016>, 2016.
1195 Shakun, J., Clark, P., He, Marcott, S.A., Mix, A. C., Liu, A., Otto-Bliesner, B., Schmittner, A.,
1196 Bards, E. 2012. Global warming preceded by increasing carbon dioxide concentrations
1197 during the last deglaciation. *Nature* 484, 49–54. <https://doi.org/10.1038/nature10915>
1198 Shakun, J.D., Lea, D.W., Lisiecki, L.E., Raymo, M.E. 2015. An 800-kyr record of global
1199 surface ocean $\delta^{18}\text{O}$ and implications for ice volume-temperature coupling. 426, 58-68.
1200 <https://doi.org/10.1016/j.epsl.2015.05.042>
1201 Sidorenko, D., Goessling, H., Koldunov, N., Scholz, P., Danilov, S., Barbi, D., Cabos, W.,
1202 Gurses, O., Harig, S., Hinrichs, C., Juricke, S., Lohmann, G., Losch, M., Mu, L.,
1203 Rackow, T., Rakowsky, N., Sein, D., Semmler, T., Shi, X., Stepanek, C., Streffing, J.,
1204 Wang, Q., Wekerle, C., Yang, H., and Jung, T.: Evaluation of FESOM2.0 Coupled to
1205 ECHAM6.3: Preindustrial and High- ResMIP Simulations, 2019. *J. Adv. Model. Earth*
1206 *Sy.*, 11, 3794–3815, <https://doi.org/10.1029/2019MS001696>
1207 Sime, L. C., K. E. Kohfeld, C. Le Quéré, E. W. Wolff, A. M. de Boer, R. M. Graham,
1208 and L. Bopp, 2013: Southern Hemisphere westerly wind changes during the Last Glacial
1209 Maximum: Model–data comparison. *Quat. Sci. Rev.*, 64, 104–
1210 120, <https://doi.org/10.1016/j.quascirev.2012.12.008>.

Deleted: ¶

1212 Sugden, D. E., N. R. J. Hulton, and R. S. Purves (2002), Modelling the inception of the
1213 Patagonian icesheet, *Quat. Int.*, 95 – 96, 55 – 64. DOI:10.1016/S0277-3791(01)00103-2
1214 Sutherland, J. L., Carrivick, J. L., Gandy, N., Shulmeister, J., Quincey, D. J., and Cornford, S. L.:
1215 Proglacial Lakes Control Glacier Geometry and Behavior During Recession. 2020.
1216 *Geophys. Res. Lett.*, 47, e2020GL088865, <https://doi.org/10.1029/2020GL088865>
1217 Tarasov, L. and Peltier, R. W.: Impact of thermomechanical ice sheet coupling on a model of the
1218 100 kyr ice age cycle. 1999. *J. Geophys. Res.-Atmos.*, 104, 9517–9545
1219 Tozer, B., Sandwell, D.T., Smith, W.H.F., Olsen, S.C., Beale, J.R., Wessel, P. Global
1220 Bathymetry and Topography at 15 Arc Sec: SRTM15+. 2019. *Earth and Space Science*.
1221 6, 10, 1847-1864. <https://doi.org/10.1029/2019EA000658>
1222 Tigchelaar, M., Timmermann, A., Friedrich, T., Heinemann, M., and Pollard, D.: Nonlinear
1223 response of the Antarctic Ice Sheet to late Quaternary Sea level and climate forcing, *The*
1224 *Cryosphere*, 13, 2615–2631, <https://doi.org/10.5194/tc-13-2615-2019>, 2019.
1225 Toggweiler, J.R., Russell, J.L., Carson, S.R. Midlatitude westerlies, atmospheric CO₂, and
1226 climate change during the ice ages. 2006. *Paleoceanography and Paleoclimatology*. 21,
1227 <https://doi.org/10.1029/2005PA001154>
1228 Troch, M., Bertrand, S., Lange, C.B., Cardenas, P., Arz, H., Pantoja-Gutierrez, S., De Pol-Holz
1229 R., Kilian, R. Glacial isostatic adjustment near the center of the former Patagonian Ice
1230 Sheet (48S) during the last 16.5 kyr. *Quaternary Science Reviews*. 277.
1231 <https://doi.org/10.1016/j.quascirev.2021.107346>
1232 Yan, Q., Wei, T., Zhang, Z. Modeling the climate sensitivity of Patagonian glaciers and their
1233 responses to climatic change during the global last glacial maximum. 2022. *Quat. Sci.*
1234 *Rev.*, 288. <https://doi.org/10.1016/j.quascirev.2022.107582>
1235 Zech, J., Terrizzano, C.M., García Morabito, E., Veit, H., Zech, R., 2017. Timing and extent of
1236 late Pleistocene glaciation in the arid Central Andes of Argentina and Chile (22°-41°S).
1237 *Geogr. Res. Lett.* 43, 697–718. <https://doi.org/10.18172/cig.3235>.
1238
1239
1240